5-2017

Effects of Grain Size and Dopants on the Irradiation Response of Actinide Oxides

Jeffrey Morgan Walters
University of Tennessee, Knoxville, jwalte18@vols.utk.edu

To the Graduate Council:

I am submitting herewith a thesis written by Jeffrey Morgan Walters entitled "Effects of Grain Size and Dopants on the Irradiation Response of Actinide Oxides." I have examined the final electronic copy of this thesis for form and content and recommend that it be accepted in partial fulfillment of the requirements for the degree of Master of Science, with a major in Nuclear Engineering.

Maik K. Lang, Major Professor

We have read this thesis and recommend its acceptance:

Lawrence H. Heilbronn, Steven Zinkle

Accepted for the Council:
Dixie L. Thompson

Vice Provost and Dean of the Graduate School

(Original signatures are on file with official student records.)

Effects of Grain Size and Dopants on the Irradiation Response of Actinide Oxides

A Thesis Presented for the

Master of Science

Degree

The University of Tennessee, Knoxville

Jeffrey Morgan Walters

May 2017

Abstract

High energy irradiation can induce physical and chemical changes in nuclear materials, impacting their properties and performance in reactor systems. Of particular interest is the radiation response of actinide oxides, such as UO_2 [Uranium Dioxide] and ThO_2 [Thorium Dioxide], as well as analogue materials such as CeO_2 [Cerium Dioxide]. During the course of reactor operations, these nuclear materials are exposed to high energy ionizing radiation in the form of nuclear fission fragments. This study simulates the extreme conditions found in a nuclear reactor by utilizing accelerated heavy ions with mass and kinetic energy comparable to fission fragments in order to examine the effects of microstructure and rare earth doping on the irradiation response of nuclear-fuel materials. Synchrotron X-ray diffraction experiments performed at the Advanced Photon Source and transmission electron microscopy were used to characterize the samples before and after ion irradiation.

The effect of grain subdivision on radiation response at the outer rim of fuel pellets is simulated through the irradiation of oxide powders of ~20 nm grain size. Structural modifications were compared to the effect of the same irradiation of oxide powders of ~1 μm [micrometer] grain size. Samples of each grain size for three materials (UO_2, ThO_2, and CeO_2) were irradiated with 945.6 MeV Au ions to fluence values ranging from 1×10^{11} [one times ten to the eleventh] – 3×10^{13} [three times ten to the thirteenth] ions/cm^2 [ions per square centimeter]. The grain size was shown to have a considerable effect on the defect-induced unit-cell expansion with an increased radiation resistance of microcrystalline samples. The highly ionizing irradiation caused additional redox effects in CeO_2 resulting in significant structural changes.

Compositional changes which occur during the course of reactor operation, due to the accumulation of heavy fission products, were simulated *via* swift heavy ion irradiation of UO_2 samples doped with an increasing amount of rare earth elements (La, Y, and Nd). These samples were irradiated along with undoped reference samples using 167 MeV Xe ions at fluences ranging from 1×10^{11}– 5×10^{14} [five times ten to the fourteenth] ions/cm^2. Initial results show that doping of rare earth elements up to 32.87 weight % does not significantly affect the radiation response as compared to undoped UO_2.

Table of Contents

List of Figures

1. Introduction

Materials used in nuclear reactors are regularly exposed to extreme conditions, due to both high energy irradiation and high temperatures in the fuel assemblies. These extreme environments require the selection of fuel materials that are tolerant of such conditions, as the damage gradually induced in these materials by their environment limits the burnups that can be achieved in nuclear fuels, thus limiting the efficiency of reactor operations. Material selection is also important for the reliability and accident tolerance of reactors, as tolerance to extreme environments prevents the breakdown of materials. Knowledge of the responses of materials to extreme environments is necessary in order to perform this selection and design fuel materials[1].

A consequence of particular interest regarding these extreme environments is the high-burnup structure in UO_2, also known as the "rim effect". This effect has been shown to be due to the electronic energy loss of fission fragments in UO_2, and is characterized by accompanying microstructural modifications in the rim of fuel pellets as the grains in the rim subdivide and form nanometric grain boundaries[1]. In particular, two distinct types of grain shapes form in the rim of the fuel pellet, polyhedral and spherical. The high burnup structure is known to be the result of self-reorganization of the material in response to extreme conditions such as those incurred during reactor operation, and experimental data have shown that the formation of the high burnup structure is the result of energy minimization in the system[1]. This has been linked to the aggregation of defects forming a dislocation network in the material[1]. Despite knowing the mechanism of the formation of the high burnup structure, the effects of this structure on the irradiation response of UO_2 and related oxides, and therefore the performance of those materials in fuel applications, is not well studied[1].

The material responses to high energy irradiation is complex, with several types of radiation effects including point-defect formation[2, 3], disordering[4], phase transitions[5, 6, 7, 8], and amorphization[9, 10]. Point-defect formation describes the process by which individual defects, in the form of self-interstitial atoms and vacancies, accumulate within the material. These defects are often created as Frenkel pairs, a paired self-interstitial and vacancy, or Schottky defects in which two paired vacancies form. Disordering occurs when irradiation induces a loss of the ordered structure in a material, and has been shown in irradiated complex metal oxides in the form of a phase transition from the ordered pyrochlore structure to the disordered defect fluorite structure. Phase transitions have been shown in many materials as an effect of irradiation, and consist of changes from one crystal structure to another. An example of this crystalline to crystalline phase transition is the transformation of a cubic to a monoclinic phase during irradiation as observed in Gd_2O_3 by Lang *et al*[8]. Lastly, amorphization occurs when the long-range crystal structure is lost, with no crystalline phase remaining in the material.

All three materials studied in the present work have the fluorite structure ($Fm\bar{3}m$), which is described by a face centered cubic lattice with additional atoms located at positions at intermediate sites inside the FCC lattice. The first symbol refers to the FCC Bravais lattice type. The remaining symbols specify the point group of the system, in which $m\bar{3}m$ refers to two mirror planes, defined as being perpendicular to the face of the lattice, and a rotoinversion plane, $\bar{3}$, meaning a rotation of $\frac{360^{\circ}}{3}$ combined with an inversion about the center. These planes are all that is necessary to describe fully the fluorite structure[11].

Even considering only the fluorite-structured actinide dioxides, which are the most common current and proposed nuclear fuels, a wide variety of factors in both material composition and irradiation conditions can influence damage formation and the radiation

tolerance of the material (i.e. the ability of materials to retain their structures and properties under irradiation). Material-specific factors include bond covalency[12], oxidation state[13], susceptibility to disordering[4], thermodynamic properties[14, 15], and grain size[8, 13], whereas irradiation condition factors include radiation type, irradiation energy spectrum, and irradiation temperature.

While the response of materials to radiation with low specific energy is relatively well-understood[1, 12], the effects of high specific energy irradiation are less well characterized. Ions travelling at low specific energy primarily scatter elastically on the target atoms (high nuclear stopping power), while ions with high specific energy primarily induce ionizations (high electronic stopping power). As such, the two produce fundamentally different effects in materials and both cannot be characterized by a single experiment. It is known that high specific energy fission fragment irradiation, consisting of particles with masses in the range of 118-160 amu and energies in the range of 170-190 MeV[16], causes significant degradation in performance over the lifetime of nuclear fuel[17]. As such, a comprehensive simulation of high energy fission fragment irradiation in conditions likely to be encountered by materials in a reactor serves to enhance our understanding of nuclear materials on a fundamental level, allowing for more accurate predictions of the lifetime response of these materials to ionizing radiation.

Fission fragment irradiation results in damage through the displacement of atoms in the material, which can result either in amorphization, phase transition, or the buildup of point-defects, most commonly in the form of Frenkel pairs. Amorphization of materials under the effects of swift heavy ion irradiation has been observed in materials such as SiO_2[41] and $La_2Ti_2O_7$[10]. The amorphization of these materials typically occur under the effects of extremely high energy irradiation, with $La_2Ti_2O_7$ has been shown to amorphize under irradiation by 2.0

GeV ^{181}Ta ions. Phase transitions due to swift heavy ion irradiation have been shown to occur in several oxide materials, such as Ln_2O_3[5]. These materials exhibit a wide variety of phases, several of which can be induced through irradiation. For Ln_2O_3 the structure evolves from the cubic C-type structure to a B-type polymorph, an X-type nonequilibrium phase, and an amorphous phase under the effects of irradiation.The buildup of point defects in materials often manifests as an increase of the unit cell parameter of the material, as observed for CeO_2[2, 13] and ThO_2[3, 13]. In these materials, the build-up of damage follows a single-impact model, in which damage accumulates linearly until an overlap of damage tracks occurs, which is characterized by a saturation of the swelling of the unit cell parameter. In these materials, spectroscopic analysis has shown that these defects do not form complex clusters, and for ThO_2 it has been shown that no change in cation valence occurs[13]. These defects cause structural distortion in the crystal, thus resulting in swelling in the material.

The interactions between the incident particle and the target material under swift heavy ion irradiation are primarily inelastic, as the high energies of fission fragment irradiation result in a significantly higher cross section for electronic interactions as opposed to nuclear interactions. These interactions cause a large initial deposition of energy by the incident ion to the electrons of the target material, resulting in an area of increased electron temperature along the ion path. This energy is then transferred from the electrons to the atomic subsystem via electron-phonon coupling, such that the atomic temperature increases as the electronic temperature decreases[18]. This process drives the formation of defects and phase transformations through atomic displacements during the period of increased atomic temperature. The formation of ion tracks due to high energy fission fragment irradiation is illustrated in Figure 1. The structure and formation of these tracks has been studied both through both experiments and simulations[23]. It

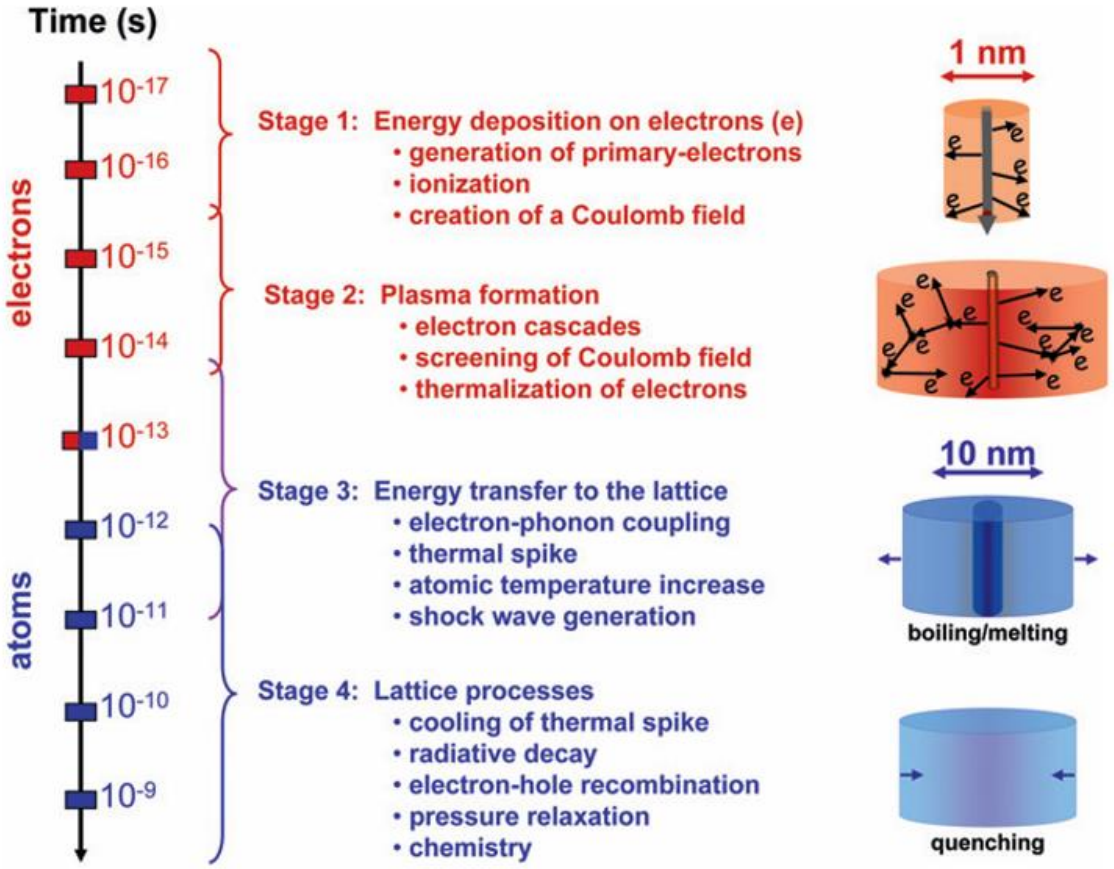

Figure 1: Schematic of the time evolution of the formation of an ion track due to nanoscale processes occurring under swift heavy ion irradiation[23].

was demonstrated that nonequilibrium phases are induced by the extreme environment created by relativistic ions within single tracks at nanometric length scales. Molecular dynamics simulations based on the thermal spike model have shown good agreement with experimental High-resolution transmission electron microscopy images of the morphology of ion tracks produced by 2.2 GeV Au ions in a variety of materials. This ion track behavior forms the basis for predictions regarding the radiation response of materials to high energy swift heavy ion irradiation.

Previous studies of the effects of fission fragment irradiation on the common nuclear fuel UO_2 by Nakae *et al.*[19] and Hayashi *et al.*[20, 21] have shown that defect production yields volume expansion, although this material retains its fluorite structure. Transmission electron microscopy (TEM) analysis was performed on these samples and confirmed an incidence region of ion implantation which was consistent with the morphological changes associated with melting, which supports the above description of energy deposition in the samples. The authors explained their findings to be largely the result of nuclear stopping at the end of the ion range. It was further shown that the volumetric expansion of the unit cell induced by irradiation was recoverable via thermal treatment with temperature ranges from 200-1000º C in three distinct steps.

More recent work by Tracy *et al.*[12] and Palomares *et al.*[22] used exposure of actinide dioxides and analogue materials to beams of swift heavy ions (SHI), which have specific energy in the range of that found for fission fragments such that electronic stopping dominates over nuclear stopping. As such, SHI were used in the current work to simulate the effects of fission fragments on the structural and chemical behavior of actinide oxides. Both unit cell expansion and phase transitions have been observed in these materials under irradiation[12], but little work

had previously been done regarding the role of nanocrystallinity in irradiation response as compared to microcrystallinity. While grain boundaries have been shown to act as defect sinks, thus improving radiation tolerance of nanocrystalline samples in the nuclear stopping regime, studies have shown that nanocrystalline materials exhibit enhanced damage under SHI irradiation[13, 41]. Nanocrystalline materials have been proposed for use in nuclear fuel, and grain subdivision in the rim effect, in which grains of size on the order of 10 μm divide into sub-micron grain[1], can generate nanocrystalline regions in conventional fuel. The modified behavior of nanocrystalline materials in response to extreme environments may have implications for understanding the high burn-up structure in nuclear fuel, which is characterized in part by these grain subdivisions. As such, a study of nanocrystalline UO_2 could provide insight into the effects of this grain subdivision on the radiation resistance of nuclear materials.

The work done by Tracy *et al.*[13] demonstrated the effects of two important material-dependent factors on the irradiation response of CeO_2 and ThO_2, the grain size and the valence of the cation. This study showed modified electronic structure in CeO_2 under the effects of swift heavy ion irradiation with 950 MeV ^{197}Au and 167 MeV ^{132}Xe. Supported by the research of Takaki *et al.*[24], whose TEM examination of ion tracks in CeO_2 demonstrated that the O anion sublattice is preferentially distorted. The authors concluded that the irradiation response of CeO_2 is primarily driven by the redox response of the Ce cation through the formation of regions of $Ce^{3+,}$ which have a lower oxygen coordination than Ce^{4+}.This maintains charge neutrality under ion irradiation. This led to an examination of nanocrystalline CeO_2, as it would be expected that redox effects would be enhanced by a reduction in grain size. In nanocrystalline CeO_2, an ion-beam induced phase transition was detected, with the initial phase no longer observed at a fluence of $5x10^{13}$ ion cm^{-2}. This new phase retains the fluorite structure, but has a significantly

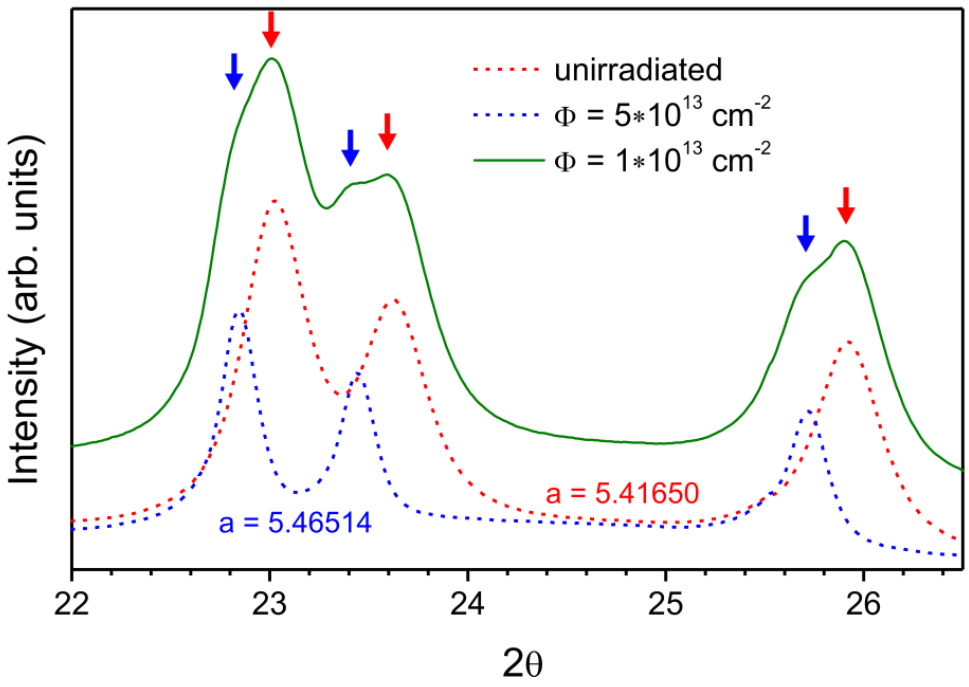

Figure 2: XRD pattern of nanocrystalline CeO_2 as a function of ion fluence. With increasing fluence, the initial peaks decrease in intensity. At the highest fluence achieved, the initial peaks are no longer observed, indicating a complete phase transition to a new fluorite material[13].

increased unit cell parameter. Similar redox effects were not observed for ThO_2, as this material has only one available valence state and does not undergo reduction[13]. This study provided important insight that the redox behavior and grain size of materials can significantly alter their irradiation response, and raises concerns regarding the use of CeO_2 as a surrogate material for the study of other actinide materials due to the specificity of the redox behavior of CeO_2.

To clarify the influence of grain size and nanocrystallinity on the response of fluorite-structured actinide dioxides to high-energy, heavy ion irradiation, the responses of microcrystalline and nanocrystalline UO_2, ThO_2, and CeO_2 to swift heavy ion irradiation have been measured by means of X-ray diffraction (XRD). This is motivated by the need to examine the differences in the effects of redox behavior and grain size among nuclear materials, in particular examining the response of UO_2 as compared to the behavior observed in CeO_2.

Further, in order to truly simulate the extreme conditions encountered by materials in a reactor, the effects of doping on the radiation response of UO_2 was considered. This is due to the implantation of fission products in nuclear fuels due to self-irradiation during the course of reactor operations. The effects of doping on actinide materials has been previously studied[25], and it was shown that doping UO_2 with oxide additives such as Cr_2O_3 and TiO_2 result in an increase in the grain size of UO_2, which is expected to increase the accident tolerance of the materials via increased fission product retention. The effect of certain dopants on the irradiation response of UO_2 has also been studied for Mg doped UO_2, Mg-Nb doped UO_2, and Ti doped UO_2[26]. These materials were irradiated to a burnup ranging from 19-94 GWd/tU at temperatures of 550-930º C. While this study directly examined the effects of these dopants on the behavior of fuel pellets under irradiation, and demonstrates the swelling of both doped and undoped fuel pellets by

irradiation, further study is required in order to determine the systematic effects of doping on nuclear materials. As such,microcrystalline UO_2 doped with Y, Nd, and La were subjected to swift heavy ion irradiation and their radiation response has been measured and compared.

Lastly, the annealing of damage caused by radiation in nuclear materials has been previously studied[19, 22], and it has been shown that increased temperature can cause annealing of the defects produced in irradiated UO_2. However, the conditions encountered by fuel in a reactor are not limited to exposure to heat after irradiation. Rather, nuclear fuel is exposed high temperature and irradiation at the same time during the course of reactor operations. In order to study this, samples of microcrystalline and nanocrystalline CeO_2, ThO_2, and UO_2 were irradiated at high temperature, and their radiation response is currently being measured and evaluated.

2. Experimental

2.1 Sample Preparation

Microcrystalline powders of UO_2, CeO_2, and ThO_2 were acquired from commercial vendors. UO_2 and ThO_2 were acquired from Ion Beam Applications Worldwide, and CeO_2 was acquired from Alfa Aesar. Nanocrystalline powders of UO_2, CeO_2, and ThO_2 were prepared by the high energy ball milling method. High energy ball milling is a widely used technique in the preparation of nanocrystalline samples, and is feasible for large-scale nanoparticle production. It is popular both due to its scalability and its low cost. High energy ball milling also leaves little residue, resulting in a high sample purity[27]. For the first sample set, both micro- and nanocrystalline powders were uniaxially pressed into holes of 100 μm diameter that were drilled into molybdenum sheets of 50 μm thickness, serving as sample holders for ion irradiation and synchrotron characterization. In general, the thickness of the molybdenum foils for this type of sample preparation can vary in size from 12.5 to 50 μm, depending on the energy of the ions used. This thickness of molybdenum foil is chosen to match the ion beam energy to allow for the beam to fully penetrate the sample pellets and inducing a homogenous energy loss.

In the case of swift heavy ions, energies of 1, 5, and 10 MeV/u correspond to sample thicknesses of 12.5, 25, and 50 μm, respectively. In order to drill these holes, a tabletop discharge machining device from Hylozoic Micro EDM System was used. This system is equipped with a 100 μm copper wire tip. Once the holes have been drilled, the molybdenum foils are cleaned in an ultrasonic bath with acetone in order to remove any debris from the drilling process. The powder samples are then placed over the holes and pressed between two steel dies using a hydraulic laboratory press using loads of ~9 tons. Following the pressing of samples, excess material is removed from the sample chamber using a scalpel under a microscope in order

to ensure that the dimensions of the pellet are as accurate and well defined as possible. For this sample set, as is typical of the preparation method, seven holes were drilled and pressed per sample material per fluence. The use of multiple pellets of sample for each fluence accommodates any potential loss of sample during irradiation and handling, such that even the loss of several pellets of sample is inconsequential to the measurement of data. For a standard beam spot size of ~1 cm^2 the holders can be prepared such that three molybdenum strips with loaded pellets can be simultaneously placed in front of the beam, such that they are all irradiated to the same fluence under the same conditions. To accomplish this, the molybdenum strips are affixed using two-sided tape to onto a larger metal plate which serves as a sample holder during the irradiation, or alternately the strips can be affixed to smaller aluminum frames, which are then mounted on the larger plate. The latter method provides the advantage of permanently fixing the strips, as the aluminum frames can be moved. Further, these aluminum frames can be individually wrapped with thin aluminum foil in order to prevent inadvertent beamline contamination due to sample loss resulting from ion-beam induced sample fragmentation[27]. The resulting sample compacts were of ~50% theoretical density, as is typical of this preparation method[13, 29].

The second sample set consisted of UO_2 powder samples doped with varying amounts of Y, La, and Nd, as well as powder samples of UC and un-doped UO_2. For the doped powders, the specific stoichiometry of the powders are as follows: $La_{0.206}U_{0.794}O_{2.158}$, $La_{0.465}U_{0.535}O_{2.1155}$, $Y_{0.194}U_{0.806}O_{2.215,}$ $Y_{0.472}U_{0.528}O_{2.038}$, $Nd_{0.196}U_{0.804}O_{2.285}$, and $Nd_{0.507}U_{0.493}O_{2.0015}$. These doped samples were synthesized by Lei Zhang and Alexandra Navrotsky at UC Davis. The synthesis of these samples was performed using a coprecipitation method, as decribed for the production of

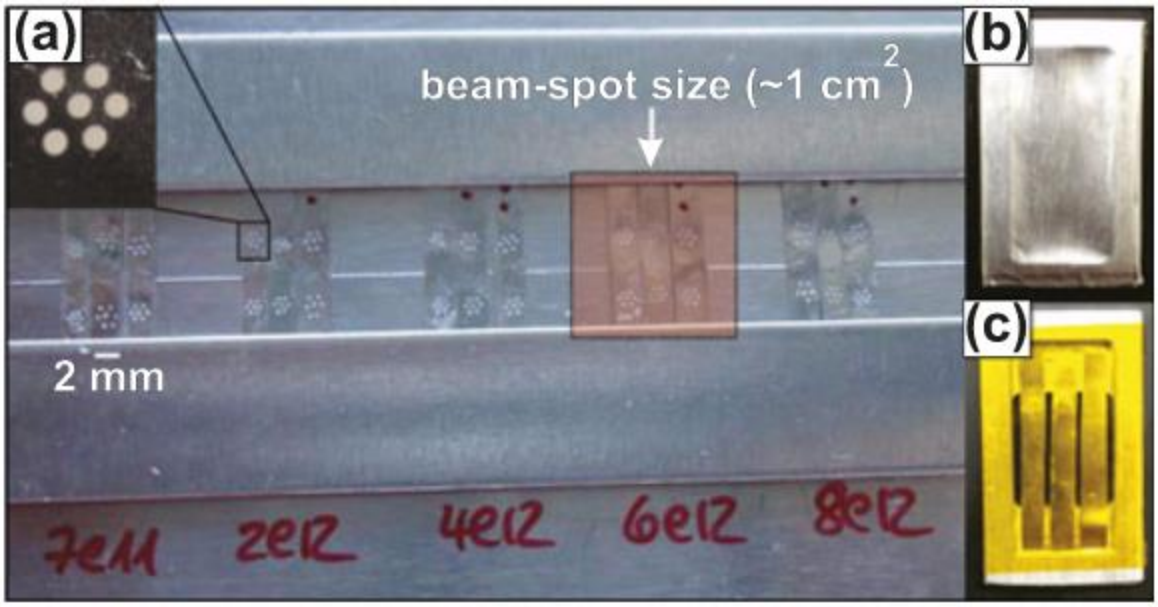

Figure 3. (a) Photograph of irradiation holder with five sets of samples for exposure to fluences from $7x10^{11}$ to $8x10^{12}$ ions cm^{-2}. Each set consists of three molybdenum strips, each with two sets of seven pellets, which are simultaneously irradiated. The inset shows the symmetrical arrangement of pellets. (b) Samples covered with thin aluminum foil in order to prevent beamline contamination. (c) Samples covered with Kapton foil for synchrotron x-ray measurements[28].

lanthanide doped urania solid solutions. Uranium nitrate and rare earth nitrate hexahydrate were mixed and dissolved in deionized water. After the dissolution, NH_4OH was added to the solution in order to reach a pH of 9-10 such that a precipitate forms.

This mixture was then stirred and heated via hot plate at ~80º C for several days to decrease the solutions volume. The remainder of the solution was then transferred into a platinum crucible and placed in a furnace to dry in air at 150º C overnight, followed by calcination in air at 600º C for 6 hours. The powder was ground in an agate mortar and pressed into pellets of 5 mm diameter, then sintered in alumina crucibles at temperatures ranging from 1100-1450 º C for 24-36 hours in a reducing atmosphere[30]. These samples were then characterized using XRD and electron probe microanalysis with wavelength dispersive spectroscopy as described in the relevant literature[30]. These samples were loaded into molybdenum strips of thickness 12.5 µm as per the procedure described above.

The third sample set consisted of the same batch of powder samples acquired for use in the first sample set, but were prepared for irradiation at high temperatures. After loading into molybdenum strips of thickness 12.5 µm, the strips were affixed in groups of three to tungsten plates using an adhesive graphite paste, as shown in figure 4. Two sets of samples were provided for each irradiation temperature, such that the second set could be heated to the same temperatures used during irradiation, but not irradiated for use as a reference sample.

2.2 Irradiation

The first set of samples was irradiated in vacuum and at room temperature at the GSI Helmholtzzentrum für Schwerionenforschung in Darmstadt, Germany using 950 MeV ^{197}Au ions from the M2 beamline of the UNILAC accelerator. Samples were irradiated to ion fluences ranging from 1×10^{11} ions cm^{-2} to 3×10^{13} ions cm^{-2}. The ion beam flux was limited to

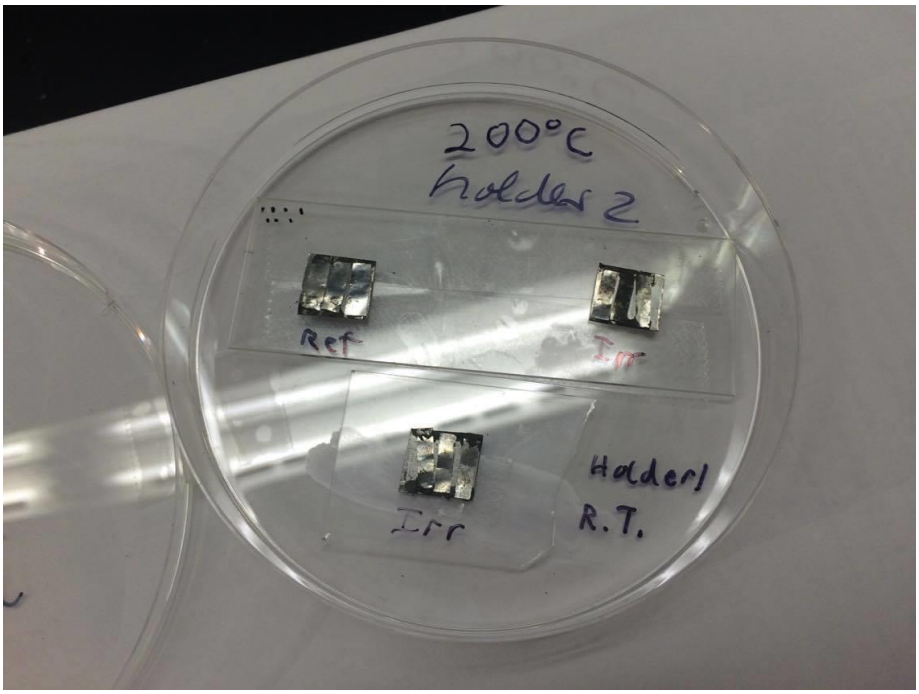

Figure 4. Three sets of three molybdenum strips each affixed to tungsten plates for high temperature irradiation. Bottom: Sample to be irradiated at room temperature. Top left: Sample to be heated to 200º C for reference. Top right: Sample to be irradiated at 200º C.

~10^9 ions cm^{-2} s^{-1} in order to avoid excessive heating of the samples. The high energy of the ion beam,

combined with the micrometer-scale thickness of the samples, ensured that ion irradiations resulted in (a) a uniform damage profile throughout the depth of the sample, (b) no ion implantation within the samples, and (c) dominant inelastic ion-matter interactions within the sample, as the electronic energy loss is significantly larger than the nuclear energy loss for the majority of the ion trajectory in the materials. The stopping power and ranges of Au ions in the material were calculated using SRIM[31] including corrections for the lower density of the samples[23]. The projected range of the ion beam was greater than the sample thickness of all the samples, such that all ions pass completely through the sample and the energy loss of the ions is nearly constant throughout the sample thickness. The range of the gold ions in each material is 70 μm in CeO_2 and ThO_2, and 64 μm in UO_2.

The second set of samples was irradiated in vacuum at room temperature using 167 MeV ^{132}Xe ions at the IC-100 cyclotron at the Joint Institute for Nuclear Research in Dubna, Russia. This sample set was irradiated to fluences ranging from $5x10^{11}$ ions cm^{-2} up to $5x10^{14}$ ions cm^{-2}. Once again, SRIM calculations were performed on the samples, all of which had projected ranges which were larger than the thickness of the sample (12.5 μm), such that the ions pass completely through the sample and no ion implantation occurs.

The third sample set was irradiated at varying temperatures to a fluence of $1.45x10^{13}$ ions cm^{-2} using 198 MeV ^{132}Xe on Cyclotron DC-60 at the Astana branch of the Institute of Nuclear Physics in Kazakhstan. The samples were divided into two groups, irradiation samples and reference samples. The irradiation samples group consisted of 4 holders irradiated at room temperature, 200º C, 400º C, and 600º C, respectively. For each sample in the irradiation group,

with the exclusion of the room temperature holder, the time that the sample was heated during irradiation was recorded. The corresponding reference sample was heated to the same temperature for the same amount of time under the same conditions, but not irradiated. This allows for a comprehensive analysis of the effects of combined heating and irradiation as compared to the isolated effects of heating the samples, which could potentially induce changes in the redox behavior.

2.3 Characterization

After irradiation, each holder was examined using an optical microscope in order to insure that radiation induced changes to the volume of the pellet or sample fragmentation have not resulted in sample loss. Once it was confirmed that there is still remaining sample material in the holders, synchrotron x-ray analysis was performed. The structure of the initial and irradiated samples was characterized using angle-dispersive X-ray diffraction (XRD) performed at the HPCAT 16BM-D beamline of the Advanced Photon Source at Argonne National Laboratory for all sample sets. At this beamline, a monochromatic x-ray beam can be configured using an adjustable Si(111) double-crystal monochromator operating in pseudo channel-cut mode. The incident beam size prior to the monochromator is 1.5 mm with a beam slit location of ~42 m from the source, resulting in an energy resolution of about $\Delta E/E = 5x10^{-4}$ at E = 25.000 keV. The beam is further focused using asymmetrical mirrors and constrained by a cleanup pinhole of 35 μm diameter. This results in an intensity on the sample of $5x10^{8}$ photons/s[28]. A monochromatic beam of 29.2 keV (λ=0.4976 Å) photons with a flux of ~10^{9} s^{-1} was used in transmission geometry for sample set one, while a beam of 25 keV (λ=0.495672 Å) was used for sample set two (add set three after APS). In order to collect XRD data, Debye-Scherrer rings are collected

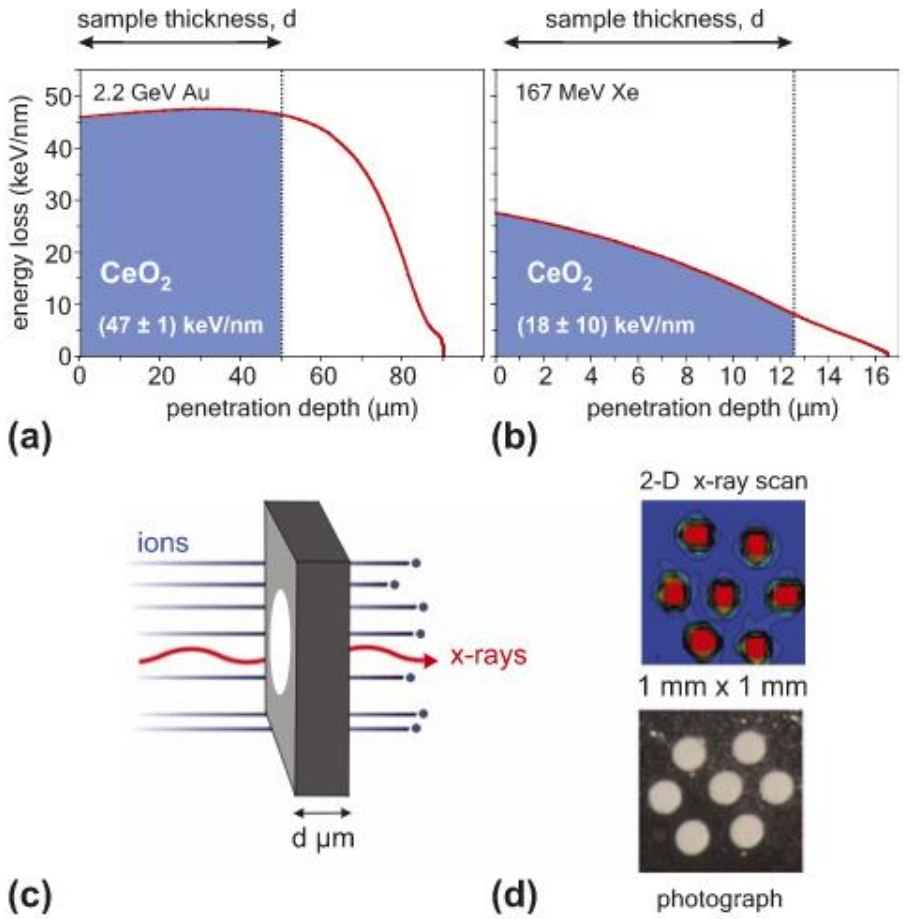

Figure 5. Energy loss of Ion Beams in CeO_2 (a) Energy loss curve for an example case of 50 μm thick CeO_2 exposed to 2.2 GeV Au ions, showing constant energy loss throughout the sample of 47 ± 1 keV nm^{-1}. (b) Energy loss curve for 12.5 μm thick CeO_2 exposed to 167 MeV Xe ions, showing larger variation in energy loss of 18 ± 10 keV nm^{-1}. (c) Schematic illustration of ion irradiation of samples and synchrotron XRD analysis. Ions completely penetrate the powder sample. The ion beam and x-rays are collinear, but the spot size of the x-ray beam is significantly smaller than that of the ion beam. (d) Two dimensional x-ray scans are used to image the sample pellets in the molybdenum foil and align the x-ray beam to find sample positions. The absorption of sample pellets is lower than that of the molybdenum strips[28].

using a MAR345 Image Plate detector, typically located 320 mm behind the sample. The detector geometry is then calibrated using a National Institute of Standards and Technology CeO_2 powder[28]. This geometry allows for the entirety of the ion tracks in a sample to be probed simultaneously, such that the resulting signal is averaged over the entire depth of the sample and is representative of the total damage caused by the irradiation of the samples. Debye-Scherrer rings were recorded using a MAR345 image plate detector with a collection time of 300 seconds. Dioptas[32] software was used to convert the diffraction images into X-ray diffractograms according to the calibration files provided by APS, and unit cell parameters were determined *via* Rietveld refinement using the Fullprof[33] software.

The average grain sizes of the unirradiated microcrystalline and nanocrystalline CeO_2 samples were determined by imaging of dispersed powders with transmission electron microscopy (TEM). Using the measured grain size and XRD patterns, the grain sizes of unirradiated nanocrystalline ThO_2 and UO_2 were calculated. The typical grain sizes of the unirradiated samples were ~1-5 μm and ~20 nm for the microcrystalline samples and nanocrystalline samples, respectively. Changes of the grain sizes in irradiated samples were determined using XRD together with calculations using the Scherrer equation[34], correcting for the initial grain size values from the TEM measurements.

3. Results and Discussion

3.1 Results

Fig. 6 shows selected XRD patterns of all measured samples at various fluences. All patterns were refined with the fluorite structure. Qualitatively, it can be seen that for all irradiated samples a peak shift to lower 2θ values occurs, indicating an expansion of the unit cell parameter, with the exception of microcrystalline UO_2. This peak shift is of a greater magnitude in the nanocrystalline samples. Further, it can be seen that nanocrystalline CeO_2 exhibits growth of a second set of peaks at high fluence values starting at $5x10^{12}$ ions/cm^2, indicating the production of a second phase under SHI irradiation. Fig. 7 shows TEM taken for unirradiated nanocrystalline CeO_2. This was used to determine the initial grain size for all nanocrystalline samples, which was measured to be 20.5±1.5 nm.

Fig. 8 shows a comparison of the change in lattice parameter among microcrystalline samples from Rietveld refinement. UO_2 demonstrates the least change in unit cell parameter among these samples, ThO_2 exhibits moderate change in unit cell parameter, and CeO_2 demonstrates the largest change in unit cell parameter. Both ThO_2 and CeO_2 follow a single impact model of damage accumulation, with saturation values of .1% and .2% change in unit cell parameter, respectively. The change in the unit cell parameter of UO_2 is too small to conclusively state that any change is occurring, as the final and initial values of unit cell parameter are within error of one another. Fig. 9 shows a similar comparison among nanocrystalline samples. From this figure it can be seen that among nanocrystalline samples, ThO_2 undergoes the lowest unit cell expansion, followed by phase 1 of CeO_2, UO_2, and finally phase 2 of CeO_2. Two notable changes occur in the nanocrystalline samples as compared to the microcrystalline samples. First, UO_2 is seen to have significant expansion of the unit cell parameter for nanocrystalline samples, as opposed to no measureable change for microcrystalline

grain size. Second, CeO_2 exhibits the growth of a second phase with increasing fluence which retains the fluorite structure, but undergoes a significant alteration in unit cell parameter, indicating much larger volumetric swelling.

A comparison of microcrystalline and nanocrystalline ThO_2 is shown in Fig. 10. It can be clearly seen that both samples of ThO_2 are damaged by the ions following a single impact model. Nanocrystalline ThO_2 demonstrates enhanced unit cell parameter expansion when compared to microcrystalline ThO_2. Fig. 11 shows a comparison of microcrystalline and nanocrystalline UO_2. While microcrystalline UO_2 undergoes no measurable change in unit cell parameter, it is shown that nanocrystalline UO_2 undergoes damage accumulation and saturation consistent with the single impact model. A comparison of microcrystalline and nanocrystalline CeO_2 is shown in Fig. 12. While it is shown that nanocrystalline CeO_2 undergoes greater unit cell expansion compared to microcrystalline CeO_2, it is also shown that nanocrystalline CeO_2 undergoes the growth of a second phase beginning at a fluence of 5×10^{12} ions cm^{-2}, which exhibits a significantly increased unit cell parameter as compared to the initial value. Lastly, the average of the fits for both phases of nanocrystalline CeO_2 is shown.

Fig. 13 shows the grain size as a function of fluence for nanocrystalline UO_2 and ThO_2. Both materials show monotonic growth of grain size with increasing fluence. Plotted lines are intended to guide the eye, and are not intended to represent a true fit to the data. Fig. 14 shows the grain size as a function of fluence for nanocrystalline CeO_2. Unlike UO_2 and ThO_2, CeO_2 undergoes a monotonic reduction of grain size as a function of increasing fluence. Again, the line is representative of the trend in the data.

Fig. 15 shows a comparison of the XRD patterns of the unirradiated doped oxide samples with the highest dopant concentrations. It can be seen that dopant has a significant effect on the

initial peak positions, which corresponds to a change in the unit cell parameter dependent on the dopant in the sample. It can be seen that for samples doped with Y and Nd, the peak shift is to larger 2θ values, indicating a decrease in unit cell parameter, while for samples doped with La the peak shift is to smaller 2θ values, indicating an increase in unit cell parameter.

Fig. 16 shows a comparison of low and high dopant concentration samples for both La-doped and Nd-doped UO_2. Here, it can be seen that the concentration of dopant directly influences the extent of peak-position change, such that higher dopant concentration results in a greater magnitude of peak shift relative to undoped UO_2. The same effect can be seen in the comparison of low and high dopant concentration Y-doped samples in Fig. 17, in which the peak shift occurs in the opposite direction. This demonstrates that an increase in dopant concentration increases the magnitude of the peak shift, while the type of dopant determines the direction of the peak shift.

Fig. 18 shows a plot of the unit cell parameter of doped samples as a function of the crystalline ionic radius of the dopant for high-doping samples. It can be seen that there is a monotonic increase in unit cell parameter with increasing crystalline ionic radius of the dopant.

Figures 19-22 show comparisons of the change in lattice parameter of samples irradiated to fluences of $7.5x10^{13}$, $1x10^{14}$, $2.5x10^{14}$, and $5x10^{14}$ ions cm^{-2}, respectively. The data allow no conclusive assessment of the effect of lanthanide doping on the radiation response of UO_2.

3.2 Discussion

Microcrystalline CeO_2, ThO_2, and UO_2 have been previously measured[13], and were expected to undergo an increase in unit cell parameter corresponding with a single impact model of damage accumulation, with the exception of UO_2, which has been shown to be extremely tolerant to ionizing radiation up to very high fluences[35]. The contribution of the present work was

to perform a systematic, comparative study of the radiation response of corresponding nanocrystalline samples. The present data show that nanocrystalline ThO_2 undergoes an enhanced damage accumulation as compared to microcrystalline samples. This behavior was also observed in nanocrystalline CeO_2 and UO_2, but with a much more significant change of their irradiation response as compared to microcrystalline samples, with the formation of a second fluorite phase for CeO_2 and the observed damage accumulation for nanocrystalline UO_2.

The increased resistance to unit cell expansion under the effect of irradiation in microcrystalline samples as compared to nanocrystalline samples can has been previously demonstrated[22, 23, 41], and can be explained using the thermal spike model. In this model, the damage track is formed via localized melting in the radius of the ion track, which occurs on the scale of a few nanometers in length. Nanocrystalline samples are more intensely effected by this damage mechanism due to the fact that the length scale of the melting event is the same as the scale of the grain size. As such, the entire grain can be melted, rather than allowing the energy to disperse through the material, as it does in microcrystalline grains.

Comparison of microcrystalline CeO_2 and ThO_2 shows that CeO_2 undergoes a larger unit cell expansion than CeO_2. As proposed in the study conducted by Tracy *et al.*[13], this is likely due to redox effects which can only occur in CeO_2. This explanation, which is supported by TEM measurements performed by Takaki *et al.*[24], states that regions of Ce^{+3} form in the material. As Ce^{+3} has a larger ionic radius than Ce^{+4}, volumetric swelling occurs due to the change in cation valence. This effect can be seen much more clearly in nanocrystalline CeO_2, in which the magnified redox effects result in the creation of a second fluorite phase. Nanocrystalline samples exhibit a more efficient loss of oxygen under SHI irradiation[13], resulting in local regions of CeO_{2+x} and CeO_{2-x}. Previous research has shown via TEM measurements that the oxygen

sublattice is preferentially distorted in CeO_2 with grain size of ~16 nm[24], which is comparable to the grain sizes examined in the current work.

The formation of the second phase of CeO_2 is driven by an enhanced redox behavior in nanocrystalline samples. Specifically, one potential explanation for this behavior is the displacement of oxygen from the region of the ion track, leading to an oxygen deficient core and an oxygen rich outer region. Since this new phase retains the fluorite structure, rather than undergoing a transition to the hexagonal structure indicative of Ce_2O_3, it is believed that these regions are composed of CeO_{2+x} and CeO_{2-x}, resulting in a region of large unit cell expansion and a region or normal unit cell expansion due to irradiation.

As ThO_2 is only stable in the tetravalent state, it is unable to undergo irradiation induced redox behavior, and so exhibits only the enhanced damage associated with nanocrystalline materials. The behavior of nanocrystalline UO_2 cannot presently be explained. U has more available oxidation states than the other materials examined, which may play a key role in the radiation response of nanocrystalline materials.

Measurements of the changes in grain size in the nanocrystalline samples of each material provide further insight into the irradiation response of these materials under high fluences. Once again, CeO_2 is shown to behave uniquely relative to ThO_2 and UO_2. The growth of grains in nanocrystalline materials has been previously observed, and so the results for ThO_2 and UO_2 are to be expected. While CeO_2 has also been shown to undergo irradiation induced grain growth[36], the degree of disorder in the material has been shown to depend on electronic energy loss. Previous studies have shown grain growth occurring under irradiation[36]. The mechanism proposed for this grain growth is the joining of separate grains via the formation of a

dislocation network. It is likely that the increased damage and oxygen loss caused by the reduction of CeO_2 results in fragmentation of grains.

While doped UO_2 has been previously studied, these studies focus primarily on the effects of dopants on the thermal properties of the materials, as well as the use of dopants used in fuel pellets, as opposed to the studied samples which were selected to simulate the doping which could occur in the material as a result of fission products produced during the course of reactor operations[37, 38, 39].

Measurements of the initial lattice parameter of unirradiated doped UO_2 samples demonstrate that the expansion or contraction of the lattice as a result of doping is directly dependent on the crystalline ionic radius of the dopant, as calculated by Shannon[40], such that dopants with an ionic radius greater than that of Uranium in UO_2 result in an expansion of the lattice and vice versa. Further, it is shown that the difference in ionic radius between Uranium and the dopant determines the magnitude of the expansion or contraction of the lattice. Thus, the unit cell parameter of the UO_2 lattice can be modified in a predictable fashion via doping with elements of various ionic radii.

This insight is furthered by the examination of the effects of dopant concentration on the peak shift in unirradiated samples. It is shown that the concentration of dopants in the sample directly influences the magnitude of the change in the unit cell parameter of the samples, implying that dopant-based control of the size of the lattice can be further tailored via manipulation of the concentration of dopants in the material. Further research in this area is warranted in order to determine the specifics of the mechanism for these modifications, as the small sample size limits the potential development of a rigorous model depicting the numeric change in lattice parameter as a function of ionic radius of the dopant and dopant concentration.

It appears, however, that the relationship between unirradiated lattice parameter and ionic radius is a linear relationship.

The examination of the change in unit cell parameter for the doped samples at high fluences demonstrated some fluctuation, but no consistent conclusions can be drawn regarding systematic effects of dopant on the radiation response of UO_2 even at the highest fluences measured. It is, therefore, clear that the level of doping examined in the current work has no significant impact on the irradiation response of microcrystalline UO_2.

4. Conclusions and Outlook

The irradiation responses of actinide dioxides and analogue materials have been shown to depend strongly on their grain sizes. Microcrystalline materials were shown to be uniformly more resistant to unit cell expansion due to irradiation than their nanocrystalline counterparts. CeO_2 exhibits unique phase behavior, involving the loss of the initial phase and the growth of a new fluorite phase with a larger unit cell parameter. This may be due to irradiation induced reduction in the material, causing grain fragmentation and the formation of a CeO_{2-x} phase in the nanocrystalline samples. The ThO_2 samples exhibited behavior consistent with previous work, demonstrating damage accumulation consistent with a single-impact model in both microcrystalline and nanocrystalline samples, as well as enhanced damage in nanocrystalline samples as compared to microcrystalline samples. Microcrystalline UO_2 was found to exhibit a high degree of resistance to irradiation damage up to the measured fluences, but nanocrystalline UO_2 exhibits a great degree of unit cell expansion, which may be related to local nonstoichiometry within the material due to the many available oxidation states.

The behavior of the UO_2 lattice in response to doping was determined to depend both on the ionic radius of the dopant and on the concentration of the dopant in the material. It was shown that whether the unit cell expands or contracts depends on if the dopant has a higher or lower ionic radius than UO_2, respectively. Further, it was shown that the magnitude of this expansion or contraction is determined by the concentration of dopants in the material. The irradiation response of doped UO_2 was shown not to be significantly impacted by the presence of dopants. The effect of dopant type and concentration on the relative change in unit cell parameter was inconclusive, and the difference in the lattice parameter of doped and undoped UO_2 at high fluences is dominated by the effect of the dopants rather than the effects of irradiation.

The results of the grain size data set are potentially applicable to the performance of nuclear fuel pellets within reactors, particularly that of advanced nanocrystalline fuels or conventional fuels which have undergone grain subdivision in the rim region (the “rim effect”). Further, the results of the doping data set have potential applications for the performance of advanced doped fuels, as well as the stability of doped UO_2 during reactor operations. A set of micro- and nanocrystalline materials have been irradiated at high temperature and are currently being measured at the Advanced Photon Source in order to more accurately represent the conditions present within a reactor, as reactor temperatures are far in excess of room temperature, at which the materials studied were irradiated. Further research is required to form a more robust simulation of the conditions within a reactor, as all of the effects studied occur simultaneously within a reactor. Further recommended experiments on this topic would include the measurement of nanocrystalline doped UO_2, the effects of high temperature on doped oxides, and the combination of all three effects in a single irradiation experiment. Further, examination of a larger doped oxide sample set with regard to dopant type and concentration would potentially allow for the development of a robust, mathematical model for the relationship between ionic radius of dopant, dopant concentration, and unit cell parameter.

References

1. Vincenzo V. Rondinella, Thierry Wiss, The high burn-up structure in nuclear fuel, Materials Today, Volume 13, Issue 12, December 2010, Pages 24-32
2. Clarissa A. Yablinsky, Ram Devanathan, Janne Pakarinen, Jian Gan, Daniel Severin, Christina Trautmann and Todd R. Allen (2015). Characterization of swift heavy ion irradiation damage in ceria. Journal of Materials Research, 30, pp 1473-1484
3. Cameron L. Tracy, J. McLain Pray, Maik Lang, Dmitry Popov, Changyong Park, Christina Trautmann, Rodney C. Ewing, Defect accumulation in ThO2 irradiated with swift heavy ions, Nuclear Instruments and Methods in Physics Research Section B: Beam Interactions with Materials and Atoms, Volume 326, 1 May 2014, Pages 169-173
4. Maik Lang, Marcel Toulemonde, Jiaming Zhang, Fuxiang Zhang, Cameron L. Tracy, Jie Lian, Zhongwu Wang, William J. Weber, Daniel Severin, Markus Bender, Christina Trautmann, Rodney C. Ewing, Swift heavy ion track formation in Gd2Zr2−xTixO7 pyrochlore: Effect of electronic energy loss, Nuclear Instruments and Methods in Physics Research Section B: Beam Interactions with Materials and Atoms, Volume 336, 1 October 2014, Pages 102-115
5. Tracy, C. L., Lang, M., Zhang, F., Trautmann, C., & Ewing, R. C. (2015). Phase transformations in Ln 2 O 3 materials irradiated with swift heavy ions, Physical Review B, Volume 92, Issue 17, 1 November 2015
6. A. Benyagoub, Phase transformations in oxides induced by swift heavy ions, Nuclear Instruments and Methods in Physics Research Section B: Beam Interactions with Materials and Atoms, Volume 245, Issue 1, April 2006, Pages 225-230

7. Benyagoub, A. and Levesque, F. and Couvreur, F. and Gibert-Mougel, C. and Dufour, C. and Paumier, E., Evidence of a phase transition induced in zirconia by high energy heavy ions, Applied Physics Letters, 77, 3197-3199 (2000)
8. Maik Lang, Fuxiang Zhang, Jiaming Zhang, Cameron L. Tracy, Alex B. Cusick, Jason VonEhr, Zhiqiang Chen, Christina Trautmann, Rodney C. Ewing, Swift heavy ion-induced phase transformation in Gd2O3, Nuclear Instruments and Methods in Physics Research Section B: Beam Interactions with Materials and Atoms, Volume 326, 1 May 2014, Pages 121-125
9. Fengyuan Lu, Jianwei Wang, Maik Lang, Marcel Toulemonde, Fereydoon Namavar Christina Trautmann, Jiaming Zhang, Rodney C. Ewing and Jie Lian, Amorphization of nanocrystalline monoclinic ZrO2 by swift heavy ion irradiation, Physical Chemistry Chemical Physics, Issue 35, 14 May 2012
10. Sulgiye Park, Maik Lang, Cameron L. Tracy, Jiaming Zhang, Fuxiang Zhang, Christina Trautmann, Patrick Kluth, Matias D. Rodriguez, Rodney C. Ewing, Swift heavy ion irradiation-induced amorphization of La2Ti2O7, Nuclear Instruments and Methods in Physics Research Section B: Beam Interactions with Materials and Atoms, Volume 326, 1 May 2014, Pages 145-149
11. Ulrich Müller, Symmetry Relations between Crystal Structures, Fachbereich Chemie, Phillips-Universität Marburg, Germany, 2008
12. Kostya Trachenko 2004 J. Phys.: Condens. Matter 16 R1491
13. Cameron L. Tracy, Maik Lang, John M. Pray, Fuxiang Zhang, Dmitry Popov, Changyong Park, Christina Trautmann, Markus Bender, Daniel Severin, Vladimir A.

Skuratov & Rodney C. Ewing, Redox response of actinide materials to highly ionizing radiation, Nature Communications 6, 27 January 2015

14. C. Ronchi, Thermophysical properties affecting safety and performance of nuclear fuel, High Temperature, Volume 45, Issue 4, Pages 552-571, July 2007
15. J.K. Fink, Thermophysical properties of uranium dioxide, Journal of Nuclear Materials, Volume 279, Issue 1, March 2000, Pages 1-18
16. J. N. Neiler, F. J. Walter, and H. W. Schmitt, Fission-Fragment Energy-Correlation Measurements for the Thermal-Neutron Fission of ^{239}Pu and ^{241}Pu, Phys. Rev., Volume 149, Issue 3, Page 894, 23 September 1966
17. J. R. Macewan, R. L. Stoute, Annealing of Irradiation-Induced Thermal Conductivity Changes in ThO_2-1.3 wt% UO_2, Journal of the American Chemical Society, Volume 52, Issue 3, Pages 160-164, March 1969
18. N Itoh, D M Duffy, S Khakshouri and A M Stoneham, Making tracks: electronic excitation roles in forming swift heavy ion tracks, Journal of Physics: Condensed Matter, Volume 21, Number 47, 5 November 2009
19. Nobuo Nakae, Yutaka Iwata, Tomoo Kirihara, Thermal recovery of defects in neutron irradiated UO2, Journal of Nuclear Materials, Volume 80, Issue 2, 1979, Pages 314-322
20. Kimio Hayashi, Hironobu Kikuchi, Kousaku Fukuda, International Conference on Actinides Radiation damage of UO2 implanted with 100 MeV iodine ions, Journal of Alloys and Compounds, Volume 213, 1994, Pages 351-353
21. Kimio Hayashi, Hironobu Kikuchi, Kousaku Fukuda, Radiation damage of UO2 by high-energy heavy ions, Journal of Nuclear Materials, Volume 248, 1 September 1997, Pages 191-195

22. Palomares, R. I., Tracy, C. L., Zhang, F., Park, C., Popov, D., Trautmann, C., Ewing, R. C. and Lang, M. (2015), In situ defect annealing of swift heavy ion irradiated CeO2 and ThO2 using synchrotron X-ray diffraction and a hydrothermal diamond anvil cell. Jnl Applied Crystallography, 48: 711–717
23. Jiaming Zhang, Lang Maik, Ewing Rodney C., Devanathan Ram, Weber William J., Toulemonde Marcel, Nanoscale phase transitions under extreme conditions within an ion track, Journal of Materials Research, Volume 25, 2010, Page 1344
24. S. Takaki, K. Yasuda, T. Yamamoto, S. Matsumura, N. Ishikawa, Atomic structure of ion tracks in Ceria, Nuclear Instruments and Methods in Physics Research Section B: Beam Interactions with Materials and Atoms, Volume 326, 1 May 2014, Pages 140-144
25. Tiankai Yao, Spencer M. Scott, Guoqing Xin, Jie Lian, TiO2 doped UO2 fuels sintered by spark plasma sintering, Journal of Nuclear Materials, Volume 469, February 2016, Pages 251-261
26. Takeo Fujino, Tetsuo Shiratori, Nobuaki Sato, Kousaku Fukuda, Kohta Yamada, Hiroyuki Serizawa, Post-irradiation examination of high burnup Mg doped UO2 in comparison with undoped UO2, Mg–Nb doped UO2 and Ti doped UO2, Journal of Nuclear Materials, Volume 297, Issue 2, August 2001, Pages 176-205
27. J.F. de Carvalho, S.N. de Medeiros, M.A. Morales, A.L. Dantas, A.S. Carriço, Synthesis of magnetite nanoparticles by high energy ball milling, Applied Surface Science, Volume 275, 15 June 2013, Pages 84-87
28. Maik Lang, Cameron L. Tracy, Raul I. Palomares, Fuxiang Zhang, Daniel Severin, Markus Bender, Christina Trautmann, Changyong Park, Vitali B. Prakapenka, Vladimir A. Skuratov and Rodney C. Ewing, Characterization of ion-induced radiation effects in

nuclear materials using synchrotron x-ray techniques, Journal of Materials Research, Volume 30, Issue 09, 2015, Pages 1366-1379

29. E. Luther, C. Necker, B. Mihaila, P. Papin, and D. Guidry, Microstructural characterization of uranium oxide, Trans. Am. Nucl. Soc. 104, 257 (2011)
30. Lei Zhang, Alexandra Navrotsky, Thermochemistry of rare earth doped uranium oxides LnxU1−xO2−0.5x+y (Ln = La, Y, Nd), Journal of Nuclear Materials, Volume 465, October 2015, Pages 682-691
31. Ziegler, J. F., Ziegler, M. D. & Biersack, J. P. SRIM – The stopping and range of ions in matter (2010). Nucl. Instrum. Methods B 268, 1818–1823 (2010).
32. Clemens Prescher , Vitali B. Prakapenka, DIOPTAS: a program for reduction of two-dimensional X-ray diffraction data and data exploration, High Pressure Research, Vol. 35, Iss. 3, 2015
33. Rodríguez-Carvajal, J. Recent developments of the program FULLPROF, Comm. Powder Diffrn (IUCr) Newslett. 26, 12–19 (2001)
34. Ciupina, V, Zamfirescu, S, Prodan, G, Evaluation of mean diameter values using Scherrer equation applied to electron diffraction images, Nato Science for Peace and Security Series C - Environmental Security, Pages 231-137, 2007
35. Hj. Matzke, P.G. Lucuta, T. Wiss, Swift heavy ion and fission damage effects in UO2, Nuclear Instruments and Methods in Physics Research Section B: Beam Interactions with Materials and Atoms, Volumes 166–167, 2 May 2000, Pages 920-926
36. Zhang Y. et al. The effect of electronic energy loss on irradiation-induced grain growth in nanocrystalline oxides. Phys. Chem. Chem. Phys. 16, 8051–8059 (2014)

37. Yuji Arita, Tsuneo Matsui, High temperature heat capacities and electrical conductivities of UO2 doped with Nd and Mg, Thermochimica Acta, Volume 267, 1 December 1995, Pages 389-396

38. Takeo Fujino, Tetsuo Shiratori, Nobuaki Sato, Kousaku Fukuda, Kohta Yamada, Hiroyuki Serizawa, Post-irradiation examination of high burnup Mg doped UO2 in comparison with undoped UO2, Mg–Nb doped UO2 and Ti doped UO2, Journal of Nuclear Materials, Volume 297, Issue 2, August 2001, Pages 176-205

39. Razdan M., Shoesmith D. W., Influence of Trivalent-Dopants on the Structural and Electrochemical Properties of Uranium Dioxide (UO2), J. Electrochem. Soc., Vol. 161, Issue 4, 2014

40. R.D. Shannon, Revised Effective Ionic Radii and Systematic Studies of Interatomic Distances in Halides and Chalcogenides, Acta Cryst. (1976). A32, 751

41. M. Backman, F. Djurabekova1, O. H. Pakarinen, K. Nordlund, L. L. Araujo, and M. C. Ridgway, Amorphization of Ge and Si nanocrystals embedded in amorphous SiO2 by ion irradiation, Phys. Rev. B 80, 144109 – Published 19 October 2009

Appendix

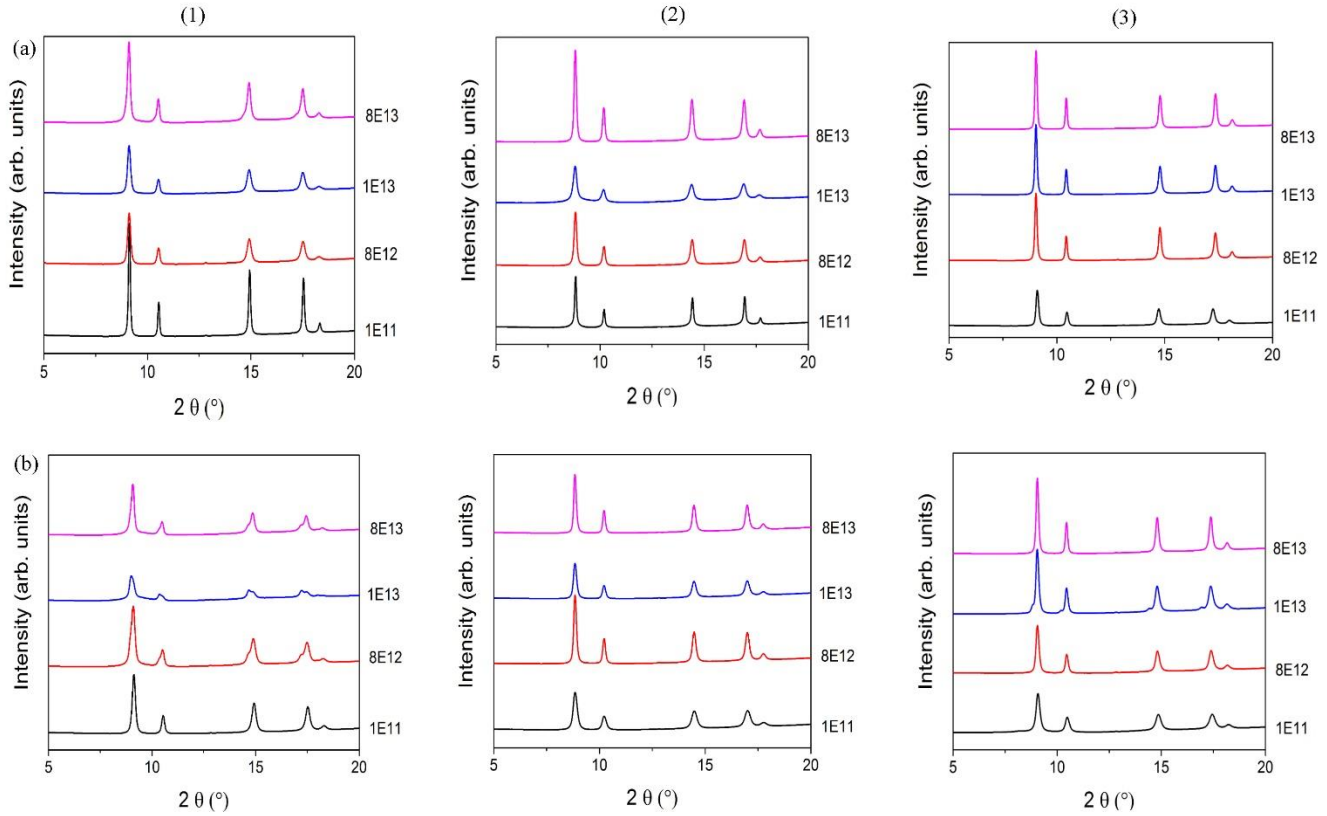

Figure 6: X-ray diffractograms of micro- (a) and nanocrystalline (b) CeO_2 (1), ThO_2 (2), and UO_2 (3)irradiated with 950 MeV ^{197}Au ions as a function of fluence. All materials exhibit fluorite structure, with peaks increasing in width and shifting to lower 2θ values with increasing fluence. This indicates unit cell expansion in the materials. Further, nanocrystalline CeO_2 exhibits the formation of a second set of fluorite-structure peaks at high fluence

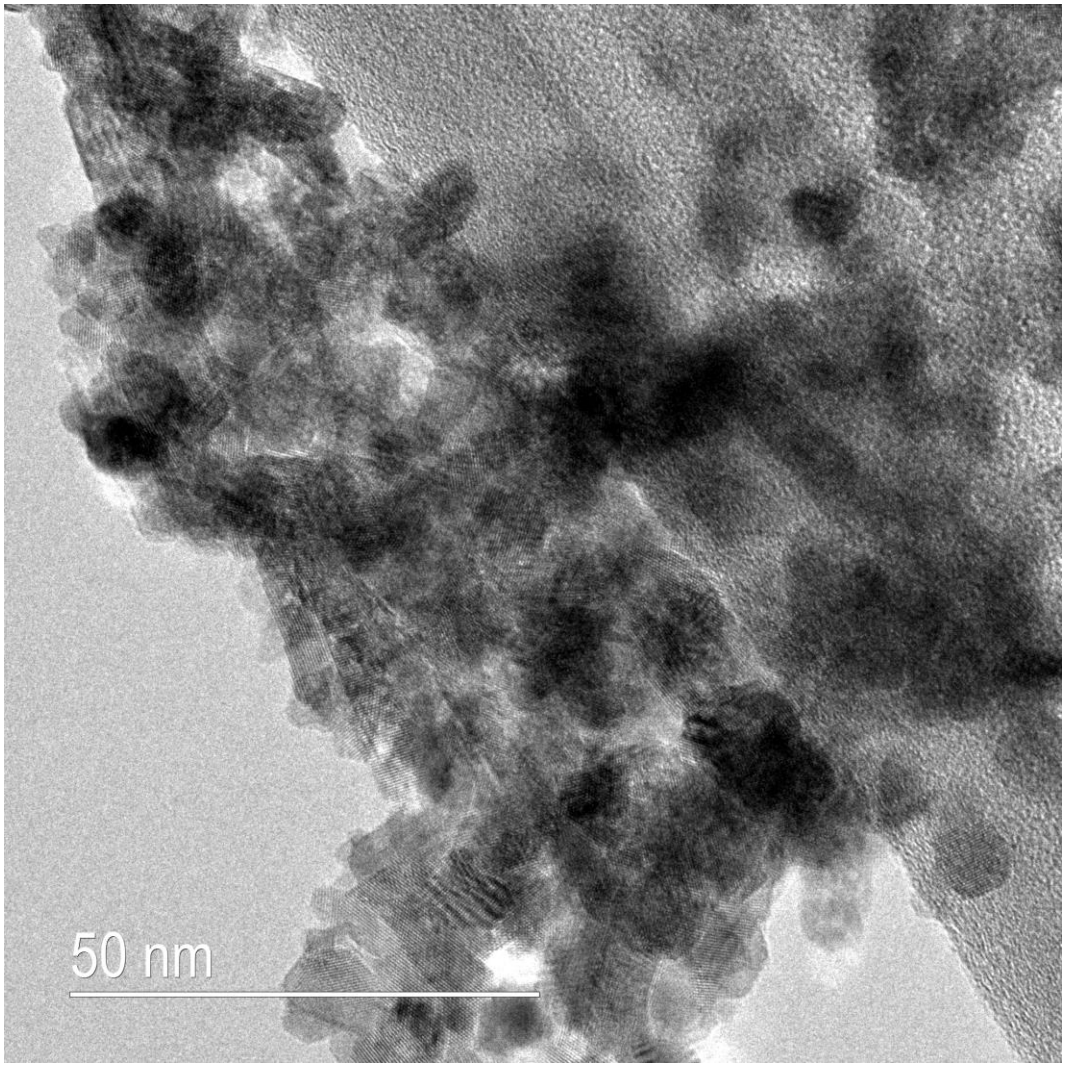

Figure 7: TEM image of nanocrystalline CeO2 was used to determine grain size. The measured grain sizes were on the order of 20 nm, which matches the value given in the prepared samples. This allows for the determination of grain growth or subdivision in irradiated samples.

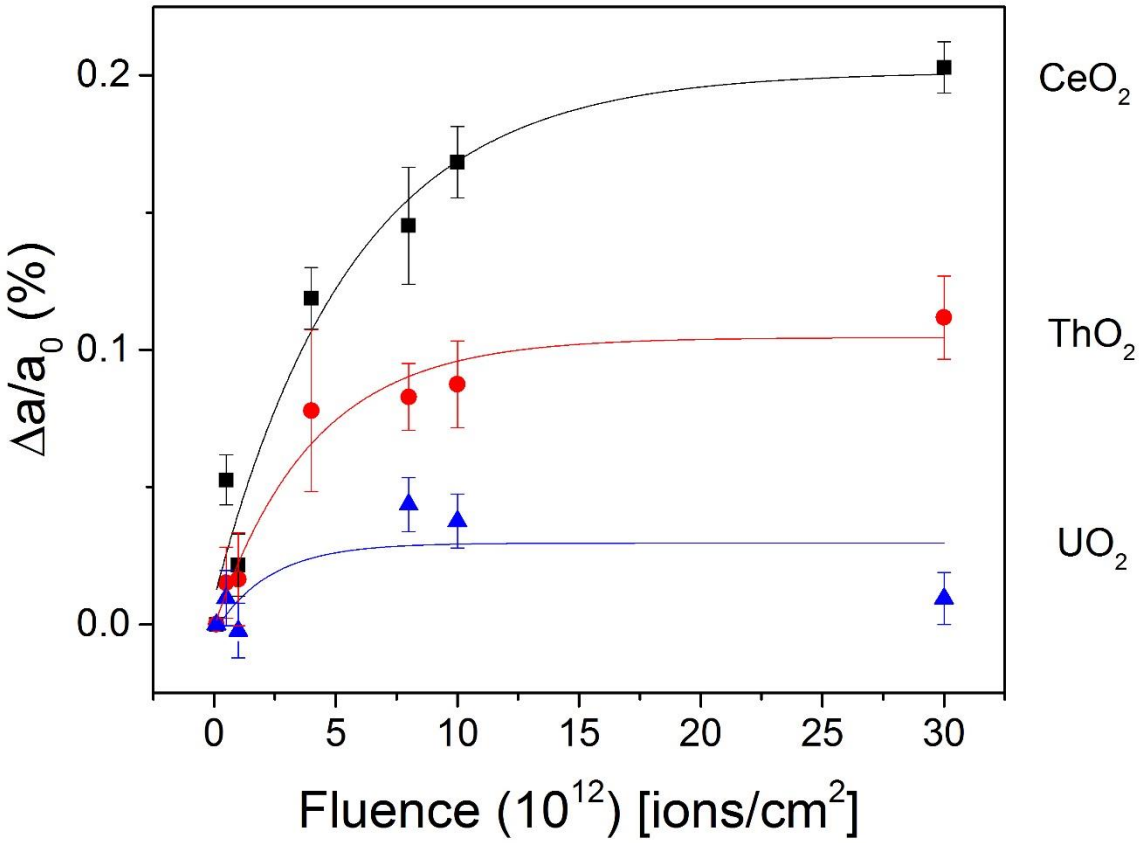

Figure 8: Change in lattice parameter relative to initial value as a function of fluence for all microcrystalline samples. UO_2 exhibits no measureable damage accumulation, while CeO_2 exhibits the most damage accumulation.

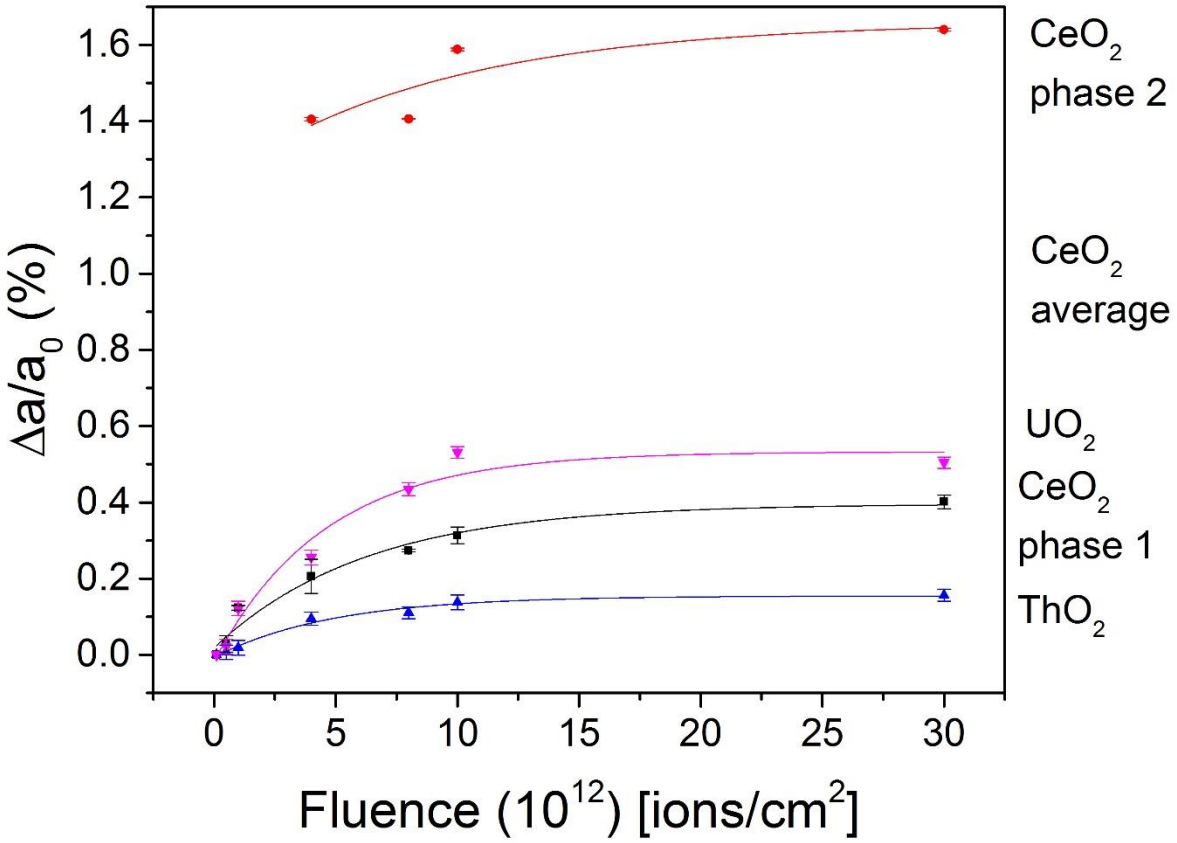

Figure 9: Change in lattice parameter as a function of fluence for all nanocrystalline samples. Comparison of nanocrystalline samples shows that UO_2, which showed the lowest increase in lattice parameter among microcrystalline samples, exhibits damage accumulation in exess of both ThO_2 and the first phase of CeO_2. The second phase of CeO_2 exhibits the most change in lattice parameter, while ThO_2 now shows the least lattice parameter expansion among all three materials.

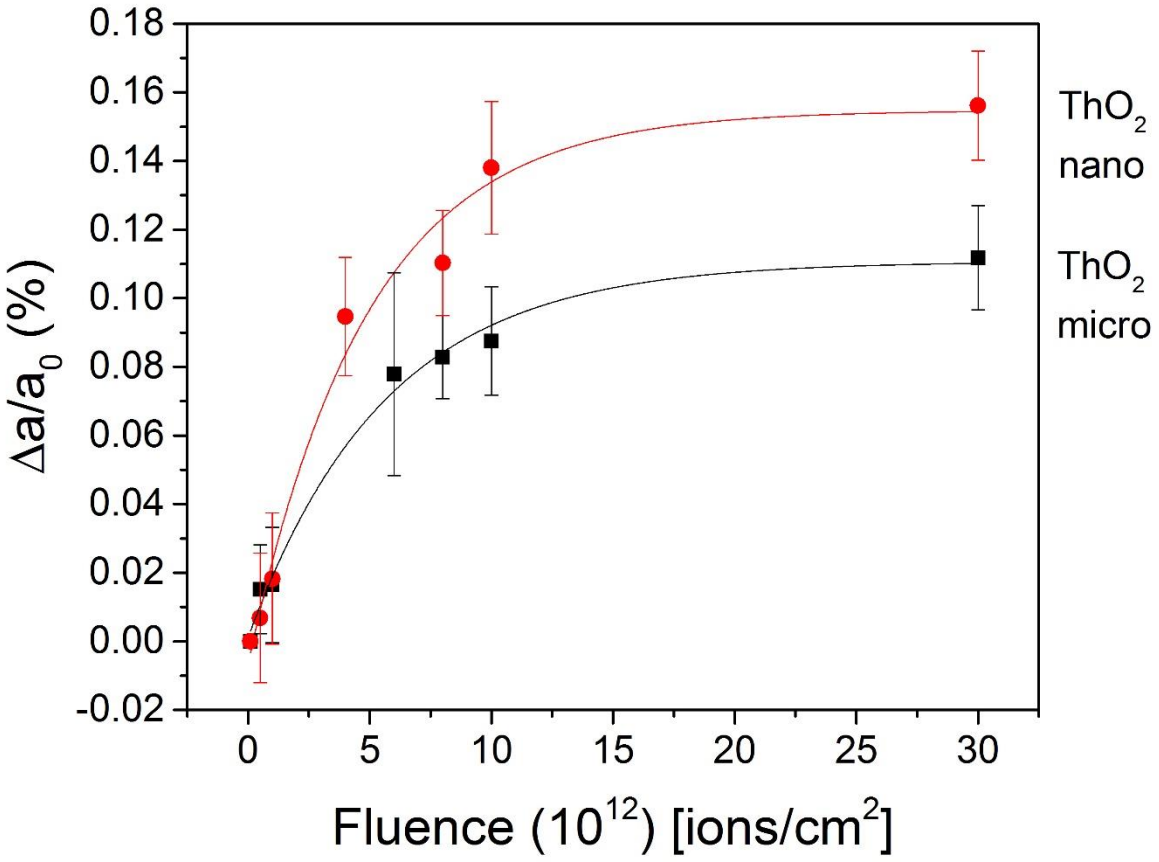

Figure 10: Change in lattice parameter relative to initial value as a function of fluence in micro- and nanocrystalline ThO_2. Both grain sizes exhibit single-impact behavior, with nanocrystalline ThO_2 being more susceptible to damage. ThO_2 demonstrates the smallest difference in the irradiation response between micro- and nanocrystalline samples.

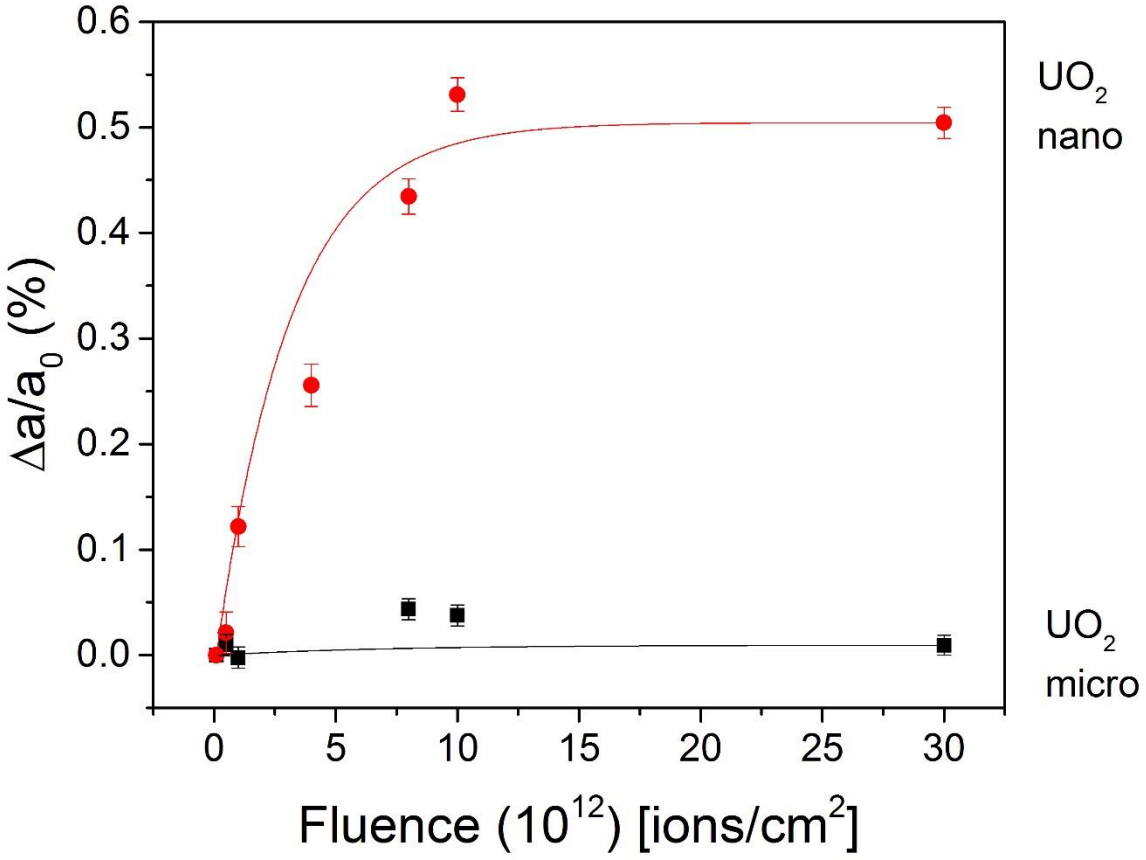

Figure 11: Change in lattice parameter relative to initial value as a function of fluence in micro- and nanocrystalline UO_2. Microcrystalline UO_2 exhibits no measureable change in lattice parameter up to the highest measured fluence, which is consistent with previous work on microcrystalline UO_2. Nanocrystalline UO_2 exhibits a significant increase in damage susceptibility over microcrystalline UO_2, constituting the greatest difference between grain sizes excluding the new phase which forms in CeO_2.

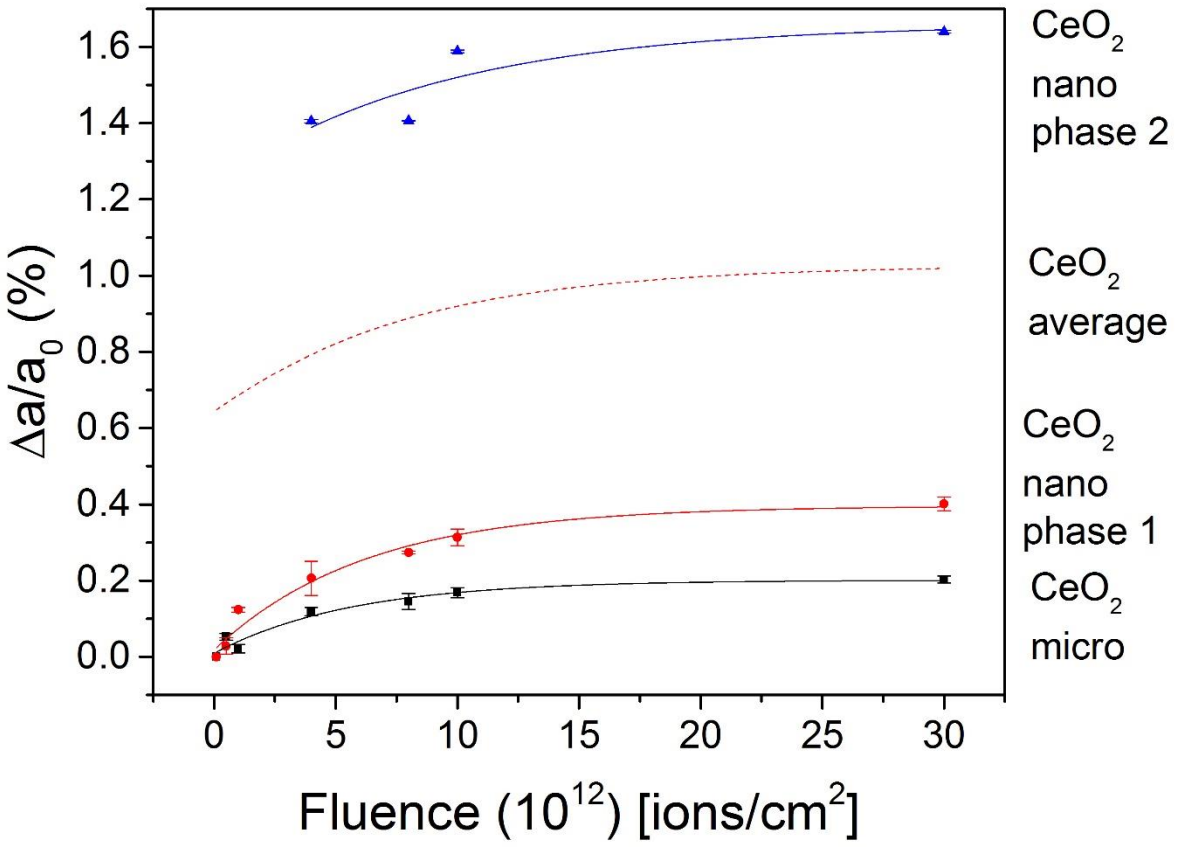

Figure 12: Change in lattice parameter relative to initial value as a function of fluence in micro- and nanocrystalline CeO_2. Both grain sizes of CeO_2 exhibit single-impact model behavior, with accumulation of damage followed by a saturation value. Nanocrystalline CeO_2 is less resistant to damage than microcrystalline CeO_2. Further, a second fluorite structured phase appears in nanocrystalline CeO_2, with a much higher relative change in lattice parameter. The average value of the fit to the two nanocrystalline phases is shown, and this value matches values measured in previous work on nanocrystalline CeO_2.

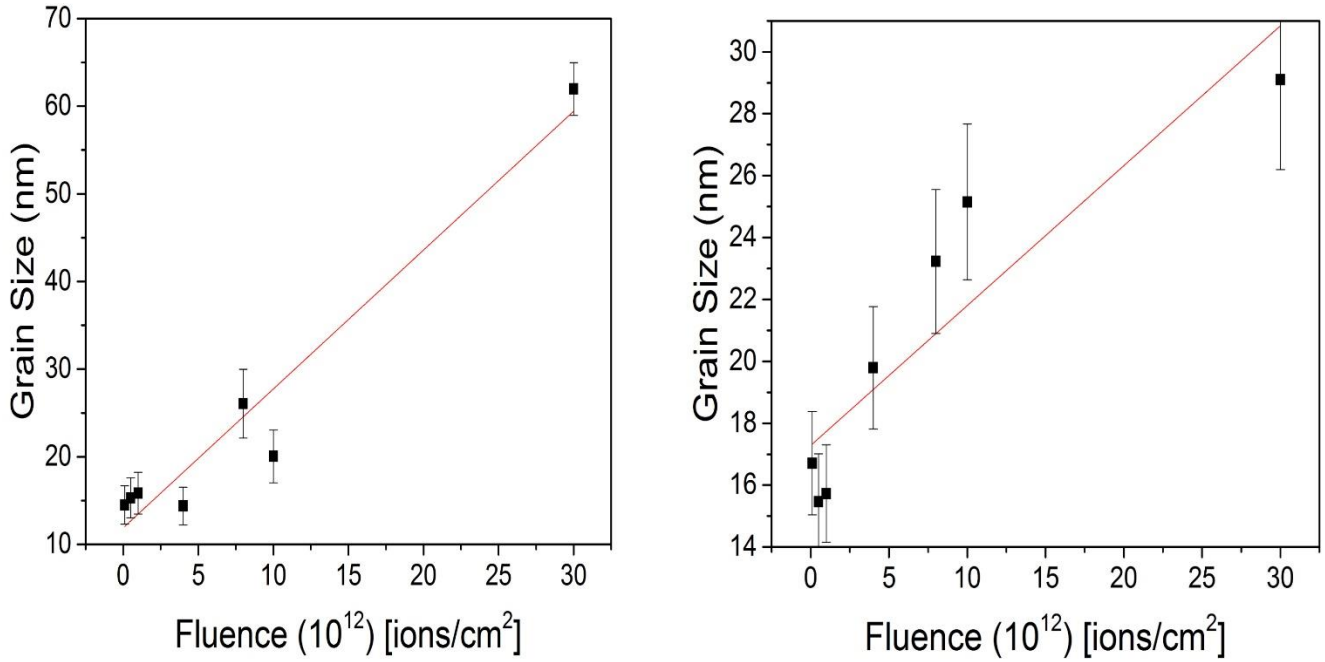

\

Figure 13: Grain size as a function of fluence for ThO_2 (a) and UO_2 (b). Both samples exhibit monotonic grain size growth under irradiation. This is consistent with other work examining nanocrystalline materials. Fits are designed to demonstrate monotonic growth, and are not representative of a linear data fit. The uncertainties in the grain sizes determined from the TEM measurements are the standard deviations of the grain ensembles that were counted

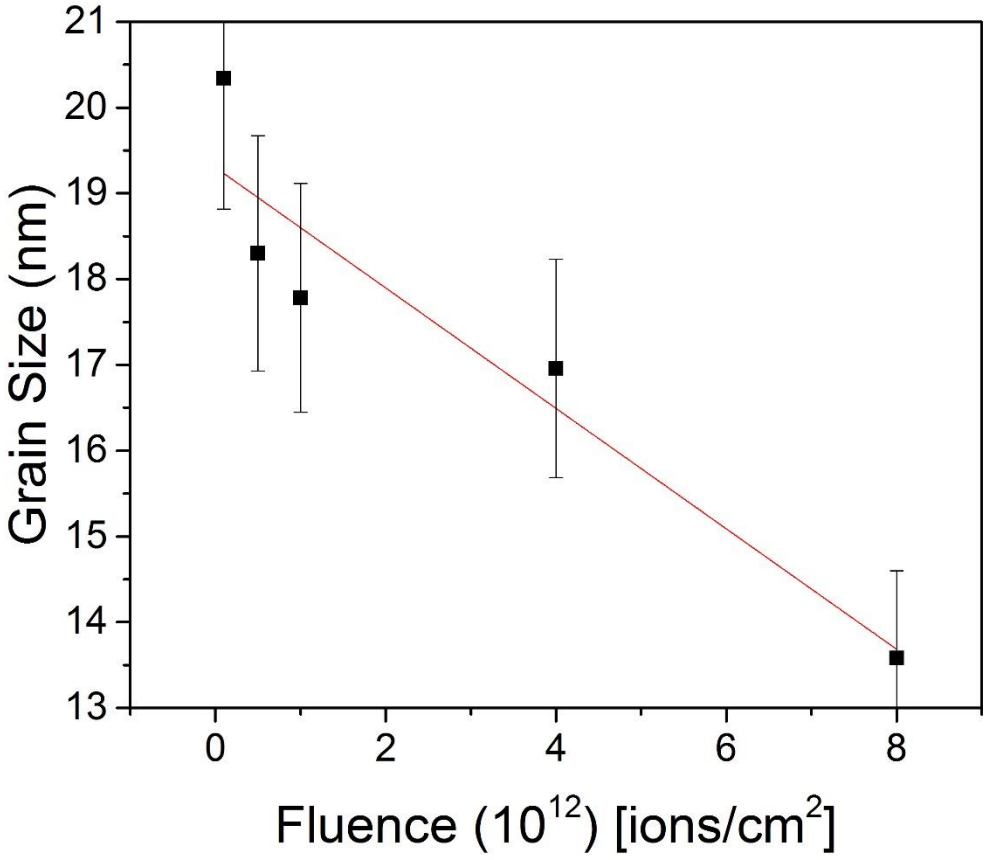

Figure 14: Grain size as a function of fluence for CeO_2. In contrast to UO_2 and ThO_2, CeO_2 exhibits monotonic decrease in grain size with increasing fluence. The formation of a second CeO_2 phase due to oxygen loss likely causes grain subdivision in CeO_2. The uncertainties in the grain sizes determined from the TEM measurements are the standard deviations of the grain ensembles that were counted.

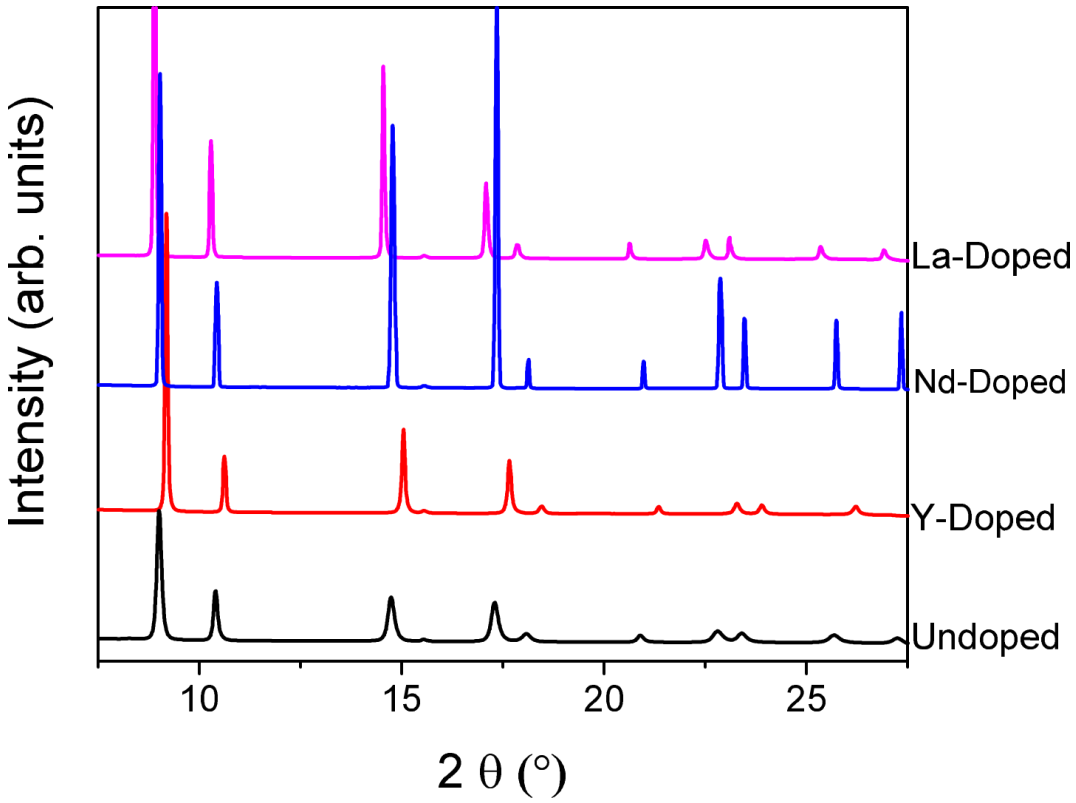

Figure 15: Comparison of XRD patterns for unirradiated samples containing high-concentration of dopants with that of unirradiated undoped UO_2. Peak shift in the XRD pattern can be seen to be heavily influenced by the type of dopant in the sample, with Y causing a shift to the right, Nd causing little change, and La causing significant shift to the left.

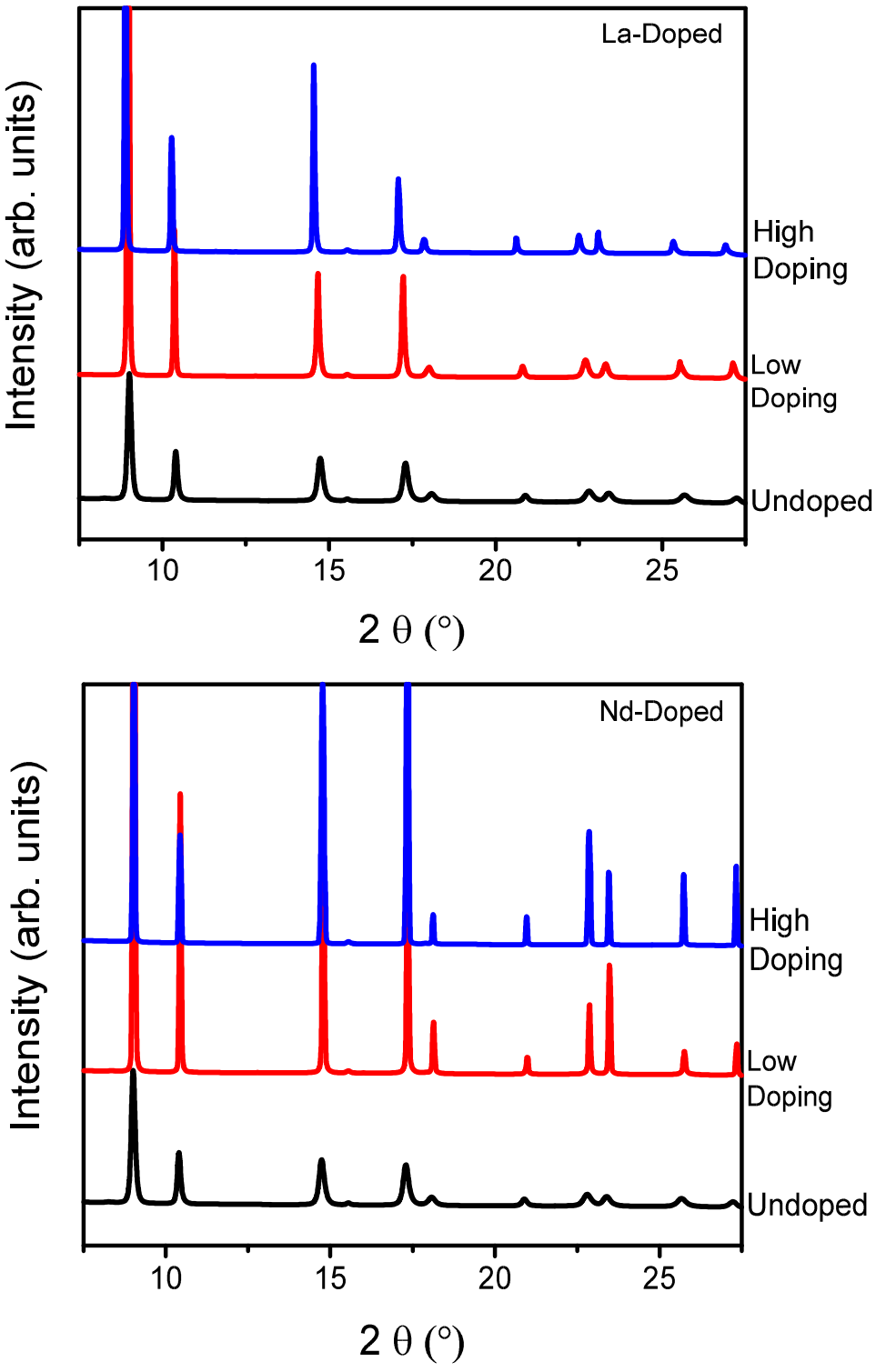

Figure 16: Comparison of XRD patterns for various dopant concentrations of Nd and La doped UO_2 with undoped UO_2. It can be seen that peak shift is directly dependent on dopant concentration.

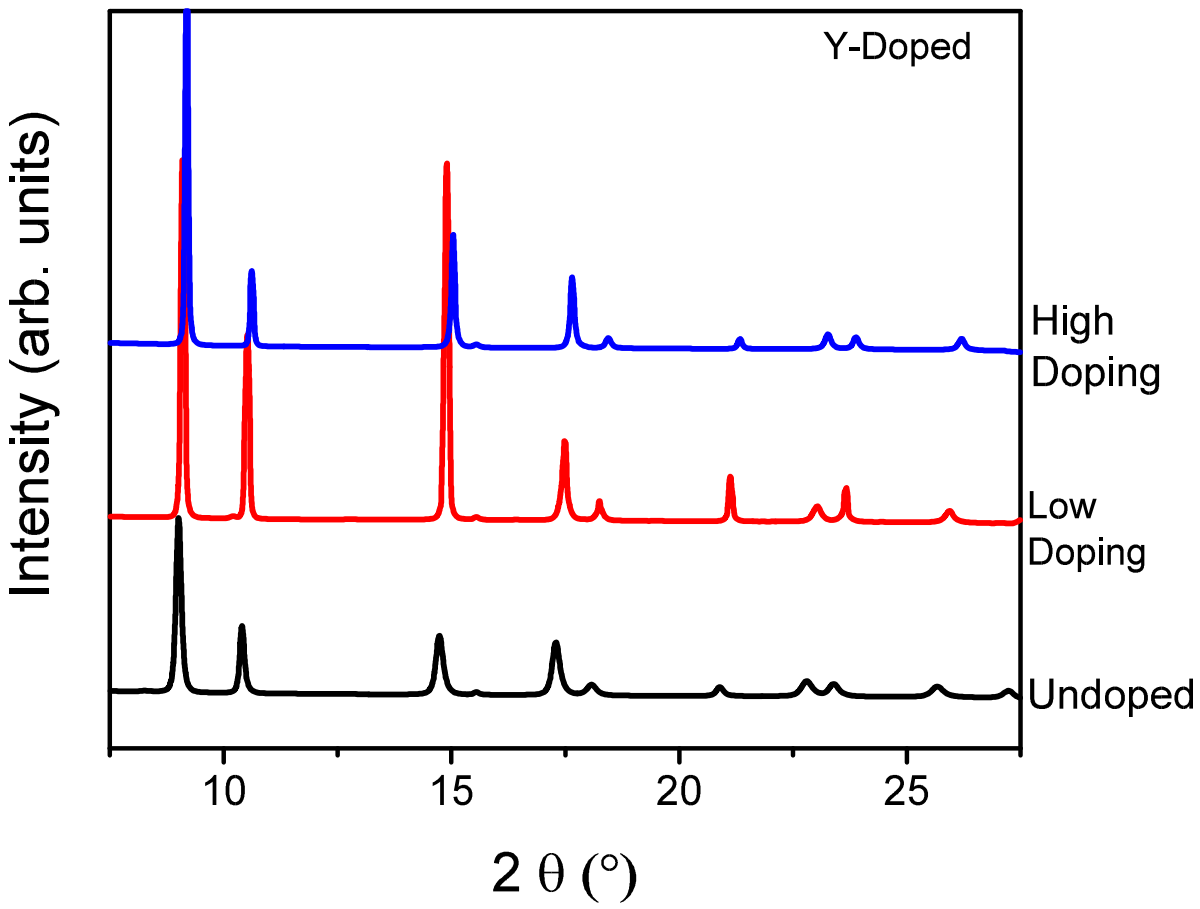

Figure 17: Comparison of XRD patterns for various dopant concentrations of Y doped UO_2 with undoped UO_2. Once again, it can be seen that magnitude of peak shift is directly dependent on concentration of dopant. When considered along with Fig. 16, it can be seen that the direction of peak shift, and to some extent magnitude, is directly dependent on the type of dopant.

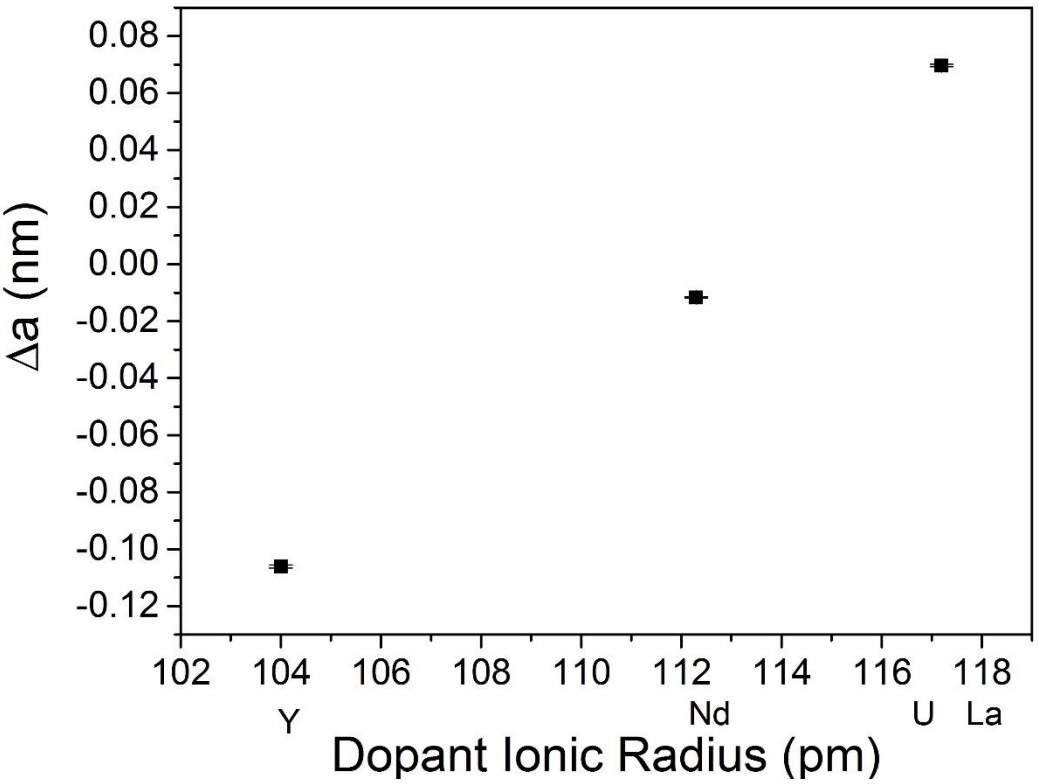

Figure 18: Change in lattice parameter of high concentration unirradiated doped UO_2 relative to the lattice parameter of undoped unirradiated UO_2 as a function of the ionic radius of the dopant. It can be seen that the change in lattice parameter is directly correlated with the ionic radius of the dopant as it compares to the ionic radius of Uranium, such that a lower ionic radius results in lower lattice parameter.

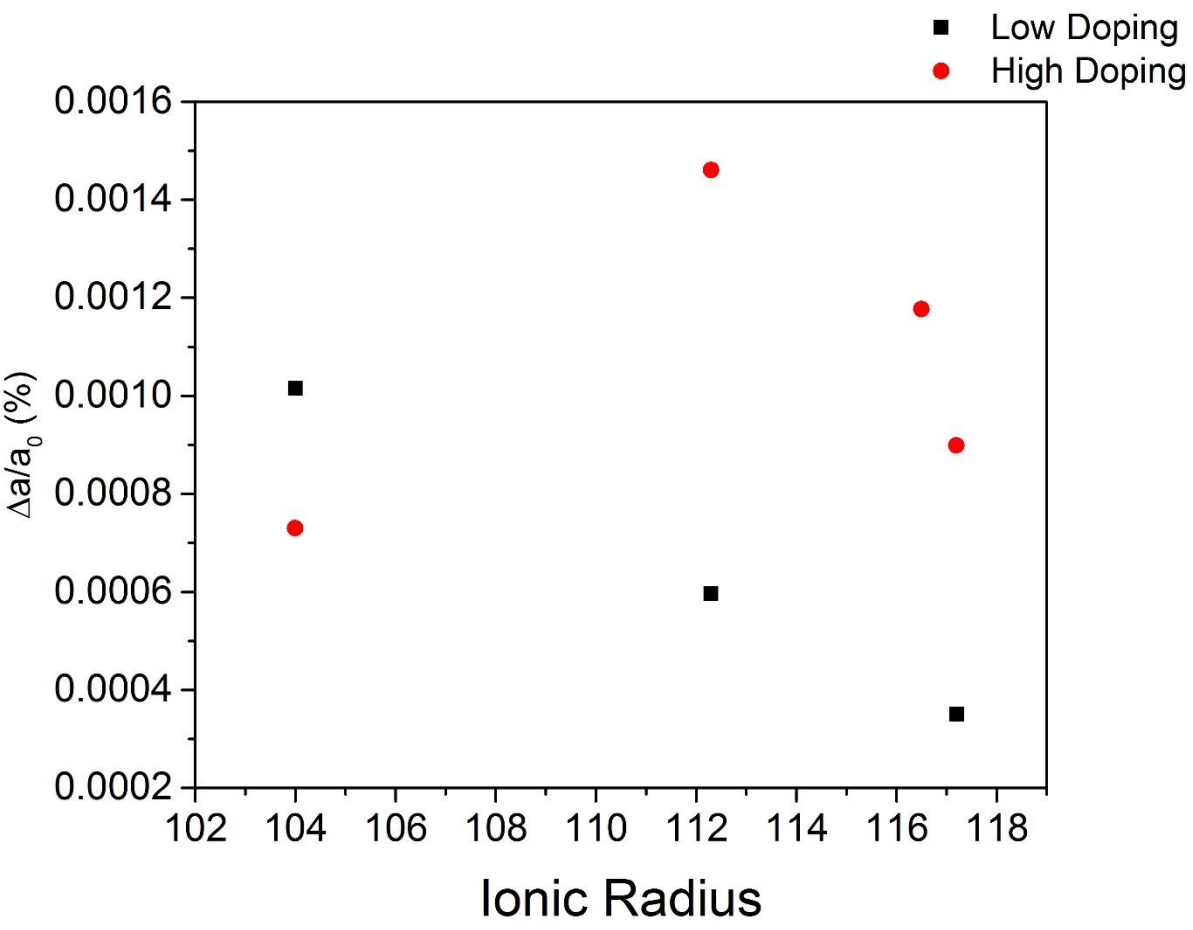

Figure 19: Change in lattice parameter as a function of ionic radius of dopant and doping concentration for doped UO_2 samples irradiated at $7.5x10^{13}$ ion cm^{-2}.

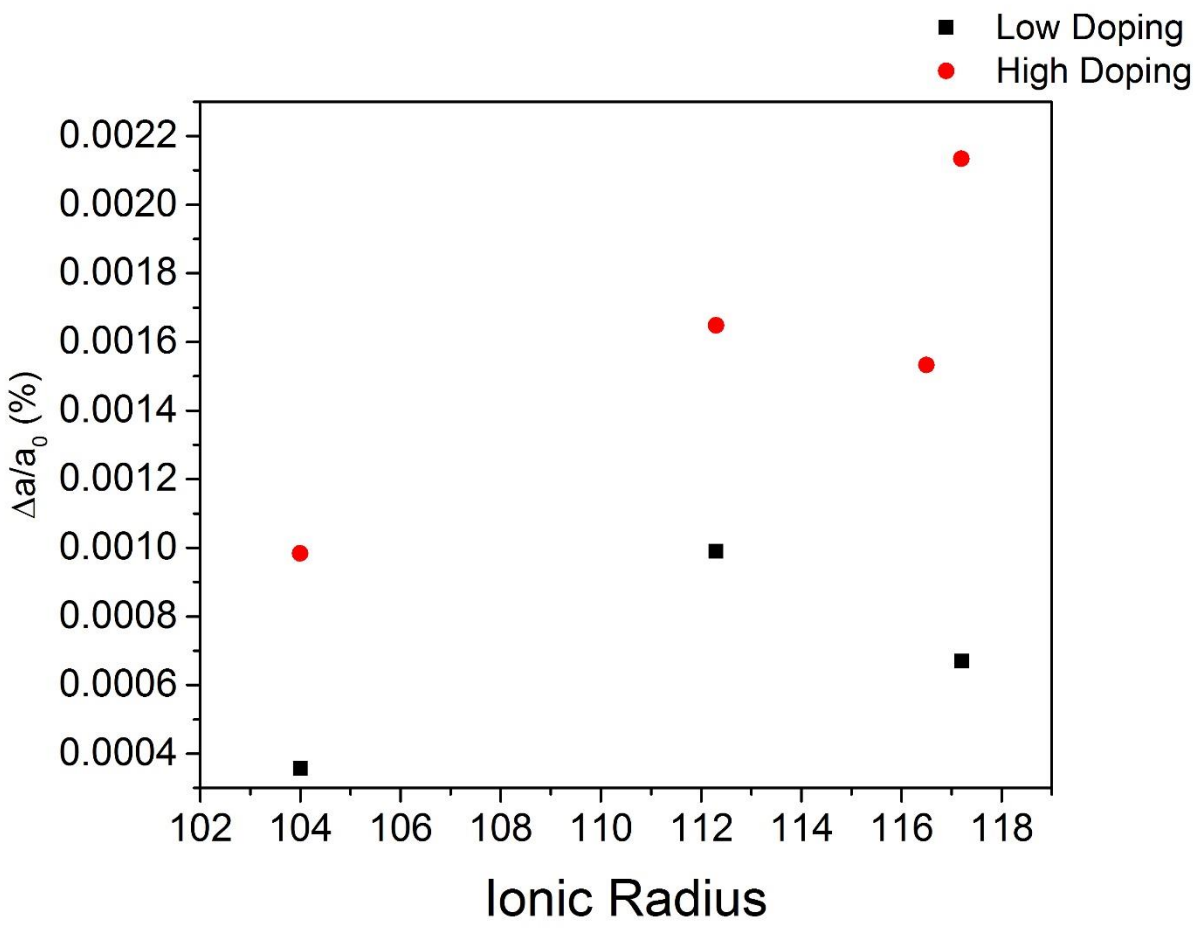

Figure 20: Change in lattice parameter as a function of ionic radius of dopant and doping concentration for doped UO_2 samples irradiated at $1x10^{14}$ ion cm^{-2}.

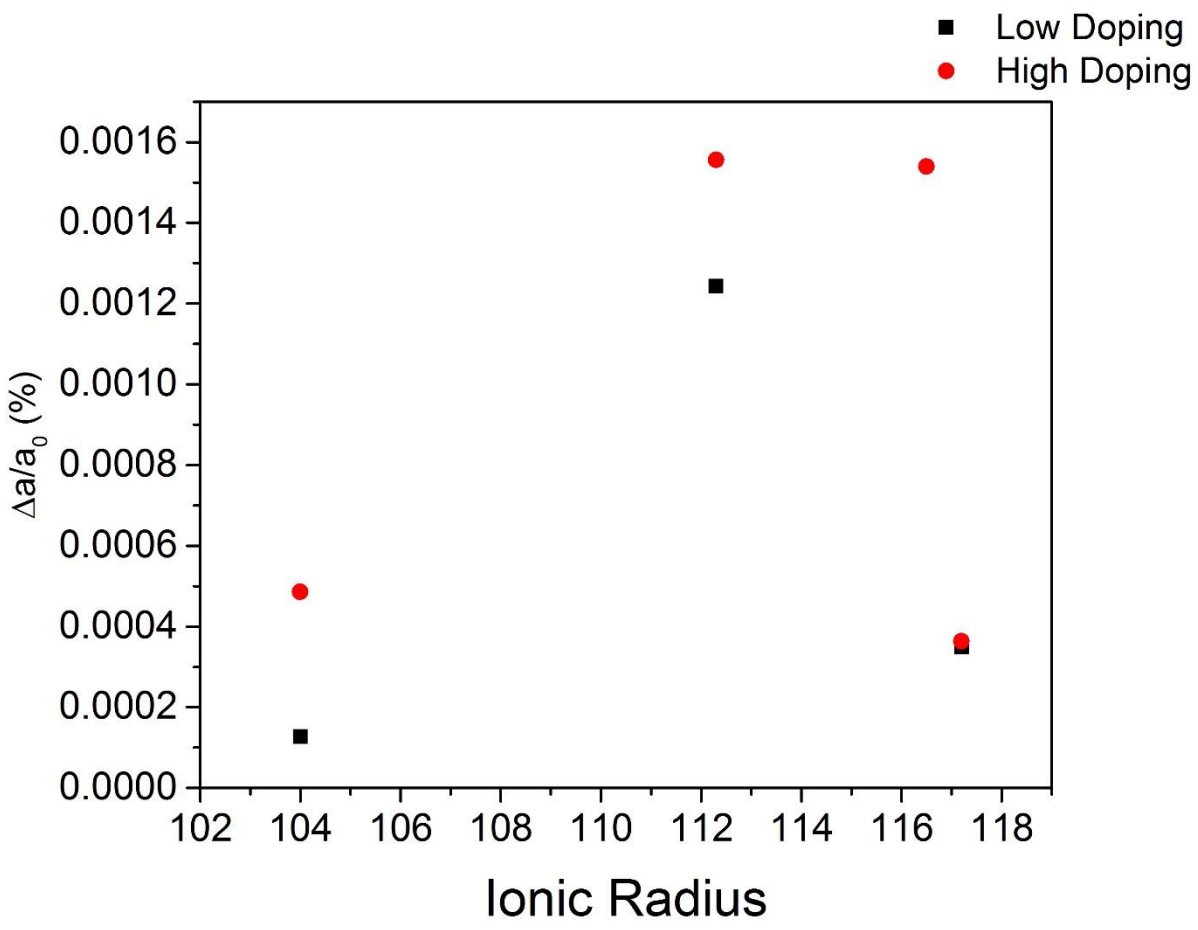

Figure 21: Change in lattice parameter as a function of ionic radius of dopant and doping concentration for doped UO_2 samples irradiated at $2.5x10^{14}$ ion cm^{-2}.

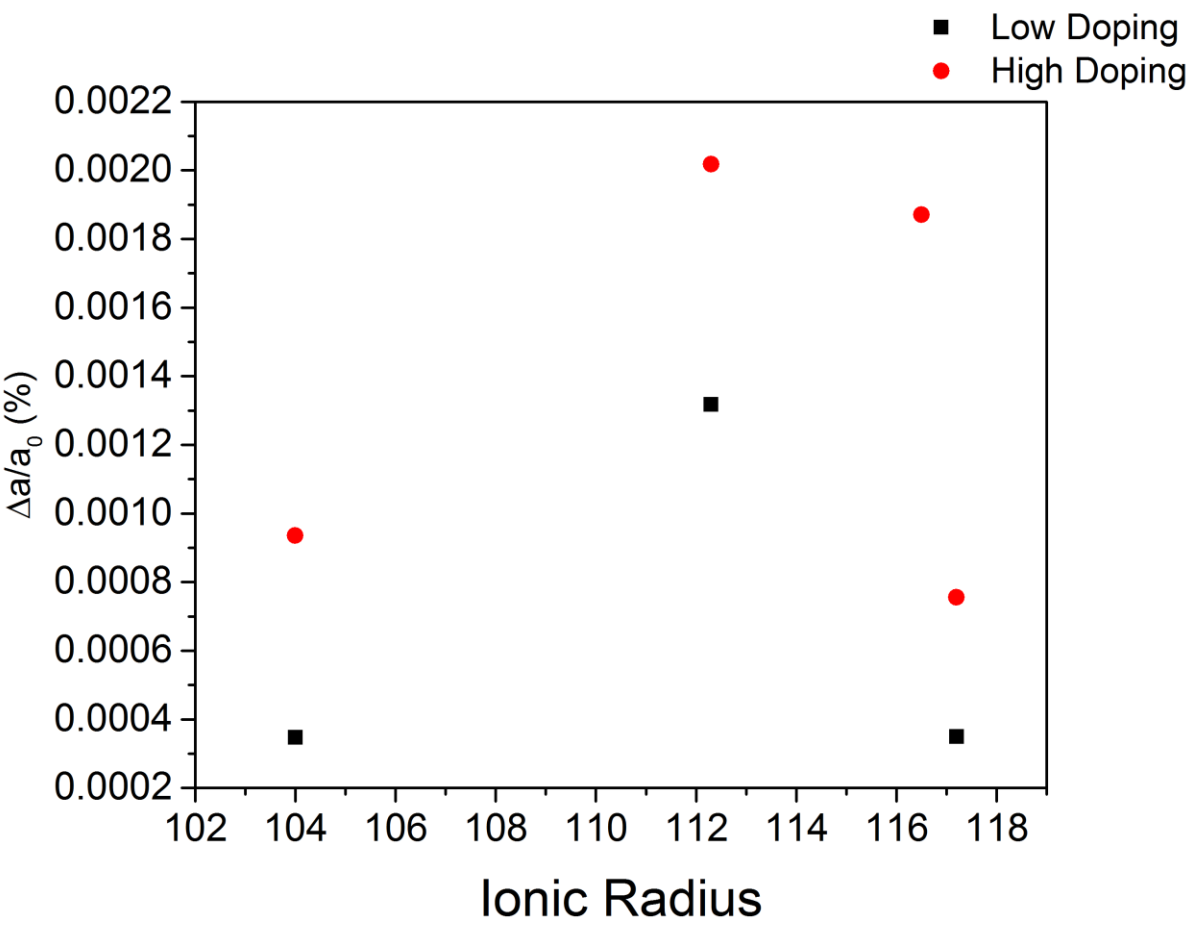

Figure 22: Change in lattice parameter as a function of ionic radius of dopant and doping concentration for doped UO_2 samples irradiated at $5x10^{14}$ ion cm^{-2}. It can be seen that higher dopant concentration consistently results in higher change in lattice parameter, though in irradiated samples there is little correlation of values for change in lattice parameter among the different dopants as a function of ionic radius. This potentially indicates that the mechanism for expansion of lattice parameter in doped irradiated samples is dependent on a more complex mechanism than the expansion of lattice parameter in undoped irradiated samples.

Vita

Jeffrey Morgan Walters was born in Pikeville, KY to parents Beverly Ann and Jeffrey Neal Walters. He attended Shelby Valley High School in Pike County, KY where he was Valedictorian. After graduation, he attended Centre College where he was a leading member of the school's chapter of the Society of Physics students and was inducted into Sigma Pi Sigma, the honors fraternity for physics students. He obtained a bachelor's degree from Centre College in May 2014 in Chemical Physics. He accepted a graduate research assistantship at the University of Tennessee, Knoxville in the Nuclear Engineering program. He graduated with a Master's of Science in Nuclear Engineering in May 2017.